Technical Memorandum 88-7

Defence Research Establishment Pacific

Centre de recherches pour la défense pacifique

The DREP Internal Wave Normal Mode Model-

Theoretical Background

39.

T.W. Dawson

April 1988

Research and Development Branch
Department of National Defence

Canada

Defence Research Establishment Pacific
Centre de recherches pour la défense pacifique

DEFENCE RESEARCH ESTABLISHMENT PACIFIC

CFB Esquimalt, FMO Victoria, B.C. VOS 1BO

DREP Technical Memorandum 88-7

THE DREP INTERNAL WAVE NORMAL MODE MODEL - THEORETICAL BACKGROUND

by

T.W. Dawson

April 1988

Approved by:

CHIEF

Research and Development Branch
Department of National Defence

Canada

ABSTRACT

This report contains the theoretical background material for a linearized internal gravity wave normal mode computational scheme implemented at the Defence Research Establishment Pacific. Currents predicted by this model have been used extensively in the production of simulated synthetic aperture radar images of internal wave signatures produced by moving vessels. A full derivation is given for the steady state internal wave fields produced by a distribution of fluid volume sources undergoing common uniform horizontal motion in a finite depth ocean. Features include a full normal mode expansion of the steady state, incorporating both the radiating internal wave field and the localized disturbance near the source. Effects of background shear are not considered. A modification of the standard eigenfunction expansion leads to accelerated convergence of the modal sums. Computation of all relevant fluid dynamical fields (3-component velocity, density, pressure and vertical particle displacement) is considered. Both sub- and super-critical source speeds can be handled. An extensive discussion of the effects of interior regions of high evanescence for certain wavenumber regimes shows how the eigenfunction expansion can be readily modified to handle such regions in a straightforward manner. The method properly accounts for trapping of energy generated within multiple thermoclines and may be of interest in certain underwater acoustics problems, where the mathematics are similar. Efficient computation of extensive sets of field data is discussed. Examples are presented for a submerged source in the N.E. Pacific Ocean. Also included is a brief comparison with measured surface-ship-generated internal wave current data.

TABLE OF CONTENTS

LIST OF TABLES

LIST OF FIGURES

1. INTRODUCTION

Much of the research effort of the Fluid Dynamics Group at D.R.E.P. has been directed towards the remote sensing of internal wave wakes using various devices, including Synthetic Aperture Radar and an Infrared Scatterometer[1]. A necessary adjunct for prediction of the performance of such devices has been a theoretical model to predict realistic internal wave current fields. These current fields may then be used to compute simulated remote sensing imagery. Applications are beyond the scope of this report, which describes the theoretical background to the internal wave computational model.

The density of the Earth's oceans is generally non-uniform, and especially so in depth, due to the effects of gravity, temperature, and salinity. This stratification of density allows the possibility of internal wave propagation due to buoyancy effects. In a stably stratified fluid, the density generally increases with depth. Thus a fluid particle which is displaced slightly up (down) will be heavier (lighter) than the surrounding fluid, and so be subject to a restoring buoyant force towards its equilibrium position. Hence any perturbation of a stably stratified ambient fluid will generally produce internal waves.

Generating mechanisms, both natural and artificial, may be of many types. The mechanisms of interest here are effects due to moving submerged bodies, which can lead to production of internal waves in several ways. One such mechanism is "wake collapse"[2,3], which involves mixing of the density by the source, followed by collapse of the density in the wake to the ambient stratified values after passage of the source. A second mechanism is the so-called "hull effect" which involves the displacement of fluid particles from their equilibrium levels due the action of the hull. This will be used for illustrative purposes later. However, the actual details of the source model have little direct bearing on the normal mode expansion which forms the core of this report.

Full computation of an internal wave field produced by a realistic submarine would be an extremely difficult task. It would require solution of the full nonlinear fluid dynamical equations, incorporating such a variety of effects as the detailed shape of the source, variations in ocean depth, ambient currents, ambient surface wind waves, effects due to the Earth's rotation and lateral boundaries, non-uniform source motions, and so on. In order to compute model internal wave fields at a reasonable cost, approximations are necessary.

It will be assumed throughout that the ocean is an incompressible, inviscid, vertically stratified[4] fluid. Effects due to the Earth's curvature and rotation will be neglected, as will non-uniform ocean depths and background currents. Thus the basic ambient state is a quiescent finite depth ocean of infinite horizontal extent.

The source model for the hull effect is taken to be a distribution of fluid volume sources. It is well-known[5] that in potential flow theory, elementary distributions of such sources in a uniform stream can produce closed streamsurfaces that resemble, and so may serve as models for, realistic hull shapes. In a linearized model, where internal wave effects are assumed small, it is expected[6] that the basic model reasonably approximates the desired rigid hull, there being minor perturbations due to the stratification. For purposes of illustrating the methods discussed in this report, the only source to be used is a simple Rankine ovoid[5,6]. However, the internal wave model has been used extensively with other source distributions.

Further approximations include linearization of the fluid dynamical fields about the ambient state, and the Boussinesq approximation[7,8]. Such approximations are used extensively[4,6,9,10] for studies of this type and provide an efficient computation scheme via a normal mode expansion technique. Finally, it is assumed that the source is in uniform horizontal motion, so that transient effects due to startup or manoeuvering of the source are not implemented in the model. Such transient effects are briefly discussed in the text, however.

This report is then basically concerned with numerical implementation of the above-mentioned normal mode expansion. As noted earlier, actual source details are of little consequence for the discussion, and an elementary source as mentioned above is used for purposes of illustration.

Section 2 presents the details of the model approximations, and the pertinent linearized fluid dynamical equations. The physical perturbation quantities of interest are the pressure, density, velocity and vertical particle displacement from equilibrium. It is shown how these may all be expressed in terms of the displacement field, which in effect serves as a generalized potential. This solution of these basic equations in Fourier space is also discussed.

Section 3 treats the solution of the basic differential equations of the displacement Fourier transform. The approach is based on a Green's function technique. Partial fraction expansion of the Green's function using complex variable theory allows extraction of the singular part in closed form. The remaining sum then has accelerated convergence over the customary[6] direct eigenfunction expansion. The section concludes with expressions for the general Fourier space solutions with an arbitrary source. These could serve as a departure point for full time-dependent computations for arbitrary sources in general motion.

Section 4 is concerned with specialization to a source which is abruptly "turned on" at t=0 and is in steady uniform horizontal translatory motion thereafter. This leads to a simplification in the general solutions. It is noted that the resulting expressions are non-singular and so could be used for time-dependent computations including transient effects due to startup.

In Section 5, expressions are derived for the ultimate steady state fields. This is accomplished by referencing coordinates to the moving source, and considering the asymptotic forms of the fields as time

progresses. The physical field solutions are reduced to double Fourier inverse contour integrals.

Section 6 is devoted to inversion of the along-track Fourier inversion via residue theory. Some preliminary discussions concerning eigenvalues are included, to be expanded in Section 7. Notes concerning general source terms include consideration of the consequences of mass conservation. The section concludes with the main results of the report, which is a complete eigenfunction expansion of the fields, expressed as a single cross-track inverse Fourier transform. The expansion includes not only terms representing the usual far-field radiated internal wave wake due to real eigenvalues, but also contributions from imaginary eigenvalues which contain near-field information toward the source extremities.

Numerical details and techniques are discussed at length in Section 7. After a general discussion of solution methods for the differential equation (which is necessary for computation of eigenvalues), the model is restricted to a multilayer type, and the advantages discussed. In particular, the method may be thought of as suitably joined local WKB approximations to the eigenfunctions, rather than a stepped approximation to a physical profile. Problems commonly arise in modelling realistic profiles which may contain interior layers or groups of layers which are highly evanescent in certain wavenumber regimes. The problems and resolution are illustrated using a simple symmetric three-layer model. It is explained how such regions can cause both multiple eigenvalues and exponential overflow on a digital computer. The exponential overflow is easily handled. Simple methods are discussed for stable computation of slightly modified eigenfunctions in the presence of such multiple zeros. Basically the standard mathematical eigenfunctions are modified by regrouping terms in the eigenfunction expansion. This is accomplished by choosing interior reference depths for integration of the eigenfunctions in a manner dependent on the profile and particular associated wavenumber. The resulting modified eigenfunction set properly accounts for channelling of energy in interior ducts and can accommodate, for example, multiple sources on opposite sides

of highly evanescent regions. A brief comment is included on the effect of such regions on "global matrix"[11] methods used in acoustics, where the mathematics is similar to that in the internal gravity wave problem. The section concludes with a discussion for setting up the integrands required for Fourier inversion. Comments for an efficient computational scheme for computing extensive sets of field points are included.

Section 8 contains examples of internal wave fields computed using the methods discussed. A slightly smoothed version of a stability (N^2) profile computed from measured summertime[12] CTD data taken at Ocean Station P (50°N,145°W) is used for the examples. This profile contains two distinct thermoclines which gives rise to some of the problems related to interior evanescence mentioned above. Results are presented for two source speeds, one of which results in purely diverging waves, whereas the other generates a transverse component. Examples are also given with the source travelling in either of the two thermoclines.

A brief comparison with measured data is considered in Section 9.

2. MODEL AND BASIC EQUATIONS

Relative to Cartesian coordinates (x,y,z), the model under consideration consists of an inviscid, adiabatic fluid of infinite horizontal (x,y) extent and of finite depth, d, in the vertical z-direction. Coordinate z measures depth positively downward from a mean free surface at z=0, in the direction of a uniform gravitational field **g**. For time t<0, the fluid is at rest and the density $\rho_o(z)$ is stratified in depth. The stratification is assumed stable, so that the density gradient $\rho_o'(z)$ is nowhere negative. Additionally, it is assumed that this gradient is bounded within the fluid, thereby requiring that the ambient density be at least continuous for 0<z<d. At time t=0, a distribution S of volume sources is introduced into the fluid, which results in the generation and subsequent evolution of an internal gravity wave field. This report is concerned with computation of the associated fluid-dynamical fields in a linear approximation.

The ambient or background state is characterized by the density $\rho_o(z)$ and pressure $p_o(z)$ which are related by[8] $p_o'(z) = g\,\rho_o(z)$, the prime denoting differentiation with respect to z. For t>0, the dynamical fields of interest are the total pressure $p_T \equiv p_o(z) + p$, the total density $\rho_T \equiv \rho_o + \rho$, the x-, y-, and z-components of velocity denoted respectively by u, v and w, and the vertical displacement (positive downwards) ζ of fluid particles from their equilibrium positions. In a linear approximation, the perturbation fields (p,ρ,u,v,w,ζ) are assumed sufficiently small that any terms involving products of two or more of these quantities may be neglected in the dynamical equations. The resulting linearized equations are[8] :

(1) Conservation of mass (volume) : $\nabla\cdot\mathbf{u} = S,$ (2.1a)

(2) Invariance of density : $\partial\rho/\partial t + \rho_o'(z)w = 0,$ (2.1b)

(3) Conservation of momentum : $\rho_o\partial\mathbf{u}/\partial t + \nabla p - \rho g\hat{\mathbf{z}} = 0,$ and (2.1c)

(4) Definition of displacement : $w = \partial\zeta/\partial t.$ (2.1d)

In these equations, $\hat{}$ denotes a unit vector along the appropriate coordinate. At this stage, all perturbation fields are functions of the four variables (x,y,z,t).

The velocity and density perturbations are readily eliminated from Equations (2.1), leaving a pair of coupled differential equations

$$\partial p/\partial z = -\rho_o(z)\ (\ N^2 + \partial^2/\partial t^2)\ \zeta, \tag{2.2a}$$

and

$$\rho_o(z)\ \partial^3\zeta/\partial t^2\partial z = \nabla_h^2\ p + \rho_o(z)\ \partial S/\partial t \tag{2.2b}$$

for the pressure and displacement. In Equations (2.2), $\nabla_h^2 \equiv \partial^2/\partial x^2+\partial^2/\partial y^2$ denotes the horizontal Laplace operator, and the Brunt-Vaisala (or intrinsic) frequency N is defined[8] by

$$N^2(z) \equiv g\ \rho_o'(z)/\rho_o(z). \tag{2.2c}$$

This fundamental quantity (N) represents the local natural frequency of oscillation of a fluid particle slightly displaced from its equilibrium position, and is real on account of earlier assumptions.

For present purposes, it proves convenient to eliminate pressure from (2.2), leaving a single equation

$$\rho_o\ (\partial^2\zeta'/\partial t^2)' + \rho_o\ \nabla_h^2\ (N^2 + \partial^2/\partial t^2)\ \zeta = (\rho_o \partial S/\partial t)' \tag{2.3}$$

for the displacement. The coefficients depend only on z, so subsequent work is simplified by application of Fourier transforms in x, y, and t. Specifically, the triple transform of a function $f(x,z,t)$ is defined by

$$\tilde{f}(k,z,\omega) \equiv \frac{1}{2\pi} \iint_{-\infty}^{\infty} d^2x\ \ e^{ik\cdot x} \int_0^{\infty} dt\ e^{-i\omega t}\ f(x,z,t), \tag{2.4a}$$

and the inverse operation is given by

$$f(\mathbf{x},z,t) = \frac{1}{4\pi^2} \iint_{-\infty}^{\infty} d^2\mathbf{k}\, e^{-i\mathbf{k}\cdot\mathbf{x}} \int_{-\infty-i\varepsilon}^{\infty-i\varepsilon} d\omega\, e^{i\omega t}\ \tilde{f}(\mathbf{k},z,\omega), \tag{2.4b}$$

where $\mathbf{x} \equiv x\hat{x}+y\hat{y}$ and $\mathbf{k} \equiv k_x\hat{x}+k_y\hat{y}$ denote horizontal position and wave-number vectors respectively, and boldface Roman type denotes a two-component vector. The wave vector $\mathbf{k}$ is initially real, whereas the frequency ω has a negative imaginary part to ensure convergence of (2.4a) for 'reasonable' source functions. Then $\tilde{f}$ will be an analytic function of ω in the half-plane Im $\omega \leq \varepsilon$, and Equation (2.4b) then guarantees quiescence prior to t=0 in keeping with the imposed initial conditions.

At this point the customary[8] Boussinesq approximation is adopted. Thus the generally small terms $\rho_o'(z)/\rho_o(z)$ are neglected in the dynamical equations, except when multiplied by g (cf N^2), in which case they represent the buoyancy forces which allow the internal waves to propagate. Equation (2.3) represents the general case. Under the Boussinesq approximation it simplifies and Fourier transforms to the simple second-order ordinary differential equation

$$\tilde{\zeta}'' - k^2 [1 - N^2(z)/\omega^2]\, \tilde{\zeta} = \tilde{S}'/(i\omega). \tag{2.5a}$$

Complete specification of the problem requires boundary conditions. An appropriate condition at the flat impermeable bottom z=d is[14] one of zero particle displacement. Under the Boussinesq approximation, attention is focused on purely internal wave motions, which will have generally negligible amplitudes at the free surface. The appropriate condition is[13] therefore one of vanishing displacement at z=0 also. The boundary conditions

$$\tilde{\zeta} = 0, \ (\ z=0,\ d\ ) \tag{2.5b}$$

and differential equation (2.5a) form a boundary value problem in the variable z for the particle displacement transform $\tilde{\zeta}$. All other fields may be computed from the solution to (2.5) using the following equations

obtained from the transformed versions of Equations (2.1) and (2.2) :

$$\text{Pressure :} \qquad \tilde{p} = -i\omega\, \rho_o(z)\, (\, i\omega\tilde{\zeta}' - \tilde{S}\,) \,/\, k^2, \tag{2.6a}$$

$$\text{Horizontal velocity :} \qquad \tilde{u}_h = k\, \tilde{p} \,/\, (\omega\rho_o), \tag{2.6b}$$

$$\text{Vertical velocity :} \qquad \tilde{w} = i\omega\, \tilde{\zeta}, \quad \text{and} \tag{2.6c}$$

$$\text{Buoyancy force :} \qquad g\tilde{\rho} = -\rho_o\, N^2\, \tilde{\zeta}. \tag{2.6d}$$

At this point, note that it follows immediately from (2.6d) and (2.4b) that in the physical domain,

$$g\, \rho(x,z,t) = -\rho_o(z)\, N^2(z)\, \zeta(x,z,t), \tag{2.7}$$

i.e. the buoyancy is directly proportional to the displacement at any fixed depth, and will not be given further consideration.

3. GENERAL SOLUTIONS OF THE BASIC EQUATIONS

The inhomogeneous boundary value problem (2.5) can be solved in a standard manner using a Green's function[4,15] approach. The Green's function appropriate to the present problem satisfies the system

$$[\ \partial^2/\partial z^2 + Q(k,c;z)\ ]\ G(k,c;z',z) = \delta(z-z'), \tag{3.1a}$$

$$G(k,c;z',0) = G(k,c;z',d) = 0, \tag{3.1b}$$

where

$$Q(k,c;z) \equiv N^2(z)/c^2 - k^2, \tag{3.2}$$

and the horizontal phase speed c is defined by

$$c^2 \equiv \omega^2 / k^2. \tag{3.3}$$

Solutions of the associated homogeneous boundary value problem

$$\phi''(z) + Q(z)\ \phi(z) = 0\ ;\quad \phi(0) = \phi(d) = 0 \tag{3.4}$$

can be used to construct the Green's function as will be shown shortly. For each fixed value of k^2, Equation (3.4) represents a standard[16] Sturm-Liouville boundary-value problem for c^{-2} and so admits a denumerable infinity of eigenvalues $c_n^{-2}(k)$ and associated eigenfunctions $\phi_n(k,z)$. The eigenvalues form an ascending sequence for each fixed k^2;

$$c_1^{-2}(k) < c_2^{-2}(k) < \ldots; \qquad c_n^{-2}(k) \to \infty\ (n\to\infty). \tag{3.5}$$

The eigenfunctions are orthogonal,

$$\int_o^d N^2(z)\ \phi_m(z)\ \phi_n(z)\ dz = \beta_n^2(k)\ \delta_{m,n}, \tag{3.6a}$$

and so the scaled eigenfunctions

$$\bar{\phi}_n(k,z) \equiv \phi_n(k,z) \;/\; \beta_n(k) \tag{3.6b}$$

constitute an orthonormal set.

The Green's function defined by (3.1) can be written in the form

$$G(k,c;z',z) = \phi_o(k,c;z_<)\, \phi_d(k,c;z_>) \;/\; \Delta(k,c), \tag{3.7}$$

where ϕ_o and ϕ_d satisfy surface and bottom "initial-value" problems specified by the homogeneous differential equation (3.4a) together with the single-point boundary conditions

$$\phi_o(k,c;0) = 0, \qquad \phi_o'(k,c;0) = 1, \tag{3.8a}$$

$$\phi_d(k,c;d) = 0, \qquad \phi_d'(k,c;d) = 1, \tag{3.8b}$$

and where $z_< = \min(z,z')$ and $z_> = \max(z,z')$. The Wronskian

$$\Delta(k,c) \equiv \phi_o(k,c;z)\, \phi_d'(k,c;z) - \phi_o'(k,c;z)\, \phi_d(k,c;z) \tag{3.9}$$

is independent of z, and so has the alternative expressions

$$\Delta(k,c) = \phi_o(k,c;d) = -\phi_d(k,c;0) \tag{3.10}$$

on account of the boundary conditions (3.8).

For each k^2, G is a meromorphic function of c^{-2} with simple poles

at zeros of the Wronskian Δ. Consequently, it admits a partial fraction expansion[15]

$$G(k,c;z',z) = G_\infty(k;z',z) + \sum_{n=1}^{\infty} \frac{c_n^4(k)}{c_n^2(k) - c^2} \left[\frac{\phi_o(k,c;z_<)\, \phi_d(k,c;z_>)}{\partial\, \Delta(k,c) \,/\, \partial\, c^{-2}} \right]_{c=c_n(k)}. \tag{3.11}$$

In this expression

$$G_\infty(k;z',z) = \sinh(kz_<) \sinh[k(z_>-d)] \,/\, [\, k \sinh(kd)\,] \tag{3.12}$$

is the solution of (3.1) when $c^{-2} = 0$ (or in the unstratified case $N = 0$). The numerator terms within the brackets of (3.11) are proportional to the eigenfunctions :

$$\phi_o(k,c_n;z) = \phi_n(k,z)\, \phi_o'(k,c_n;0) \,/\, \phi_n'(k,0), \tag{3.13a}$$

$$\phi_d(k,c_n;z) = \phi_n(k,z)\, \phi_d'(k,c_n;0) \,/\, \phi_n'(k,0). \tag{3.13b}$$

The Wronskian derivative in the denominator of (3.11) can be expressed in terms of an integral as follows[17]. Let "$\dot{}$" denote differentiation with respect to a parameter (not z) to be made definite later. Then from the differential equation (3.4) and its parametric derivative, the following results may be derived ;

$$(\dot\phi_d\, \phi_o' - \phi_o\, \dot\phi_d')' = \dot Q \phi_o \phi_d, \tag{3.14a}$$

$$(\dot\phi_o\, \phi_d' - \phi_d\, \dot\phi_o')' = \dot Q \phi_d \phi_d, \tag{3.14b}$$

Integration with respect to z of (3.14b) over $0<z<z'$ and of (3.14a) over $z'<z<d$, and subsequent addition of the results shows that

$$\int_o^d \dot Q \phi_o \phi_d dz = \dot\Delta + \dot\phi_d(d)\phi_o'(d) - \phi_o(d)\dot\phi_d'(d)\ \dot\phi_o(0)\phi_d'(0) + \phi_d(0)\dot\phi_o'(0).$$

The final four terms all vanish due to the boundary conditions (3.8), resulting in the simple integral relationship

$$\dot{\Delta}(k,c) = \int_o^d \dot{Q}(k,c;z)\ \phi_o(k,c;z)\ \phi_d(k,c;z)\ dz. \tag{3.15}$$

If the unspecified parameter is taken to be c^{-2}, then it is found that $\partial\Delta/\partial c^{-2} = \int_o^d N^2\ \phi_o\ \phi_d\ dz$. Substitution into (3.11) and subsequent application of (3.13) and (3.6) leads to the (modified) eigenfunction expansion :

$$G(k,c;z',z) = G_\infty(k;z',z) + G_R(k,c;z',z) \tag{3.16a}$$

where

$$G_R(k,c;z',z) = \sum_{n=1}^{\infty} c_n^4(k)\ \bar{\phi}_n(k,z)\ \bar{\phi}_n(k,z')\ /\ [\ c_n^2(k) - c^2] \tag{3.16b}$$

and where G_∞ is given in closed form by (3.12). Application of a direct eigenfunction expansion[4,6] solution of (3.1) leads to an expression identical to (3.16), but with the leading term G_∞ absent, and the numerator factor c_n^4 replaced by $c^2c_n^2$, i.e.

$$G\ (k,c;z',z) = \sum_{n=1}^{\infty} c^2\ c_n^2(k)\ \bar{\phi}_n(k,z')\ \bar{\phi}_n(k,z)\ /\ [\ c_n^2(k) - c^2]$$

Combination of this result with (3.16) leads to the identity

$$G_\infty(k;z',z) = \sum_{n=1}^{\infty} c_n^2(k)\ \bar{\phi}_n(k,z)\ \bar{\phi}_n(k,z')\ . \tag{3.17}$$

The left-hand side is independent of the profile N by (3.12). This identity could be used to check the eigenfunctions computed for a general N^2 profile.

The advantages of (3.16) over the standard expansion are its more rapid convergence, and extraction of the singular behaviour in z. The term G_∞ alone accounts for the $\delta(z-z')$ term in (3.11). Standard[15] asymptotic

results for fixed k and $n\to\infty$ show that

$$c_n^{-2} \sim n^2\pi^2/\psi^2(d) \quad \text{and} \tag{3.18a}$$

$$\phi_n(k,z) \sim \sin[\, n\pi\psi(z)/\psi(d)]/\sqrt{N(z)}, \tag{3.18b}$$

where

$$\psi(z) \equiv \int_o^z N(z')\, dz'. \tag{3.18c}$$

Thus $c_n = O(n^{-1})$, $\phi_n = O(1)$, $\phi_n' = O(n)$, etc., and the convergence rate of (3.16) is proportional to n^{-4}. Consequently up to two z or z' derivatives may be taken 'under the summation sign' in (3.16) while retaining absolute convergence of the resulting sum. The convergence rate of the standard expansion is n^{-2}. A single derivative reduces this rate to conditional, and a second derivative reduces the convergence to purely oscillatory, as is required to produce the δ-singularity of (3.1). This singular nature is carried in the isolated term of (3.16), a fact reflected in the enhanced convergence rate of the associated sum.

In terms of the Green's function, the desired solution to Equation (2.5) is

$$\tilde{\zeta}(k,z,\omega) = \int_o^d G(k,c;z,z')\, \tilde{S}'(k,z',\omega) \,/\, (i\omega)\, dz'. \tag{3.19}$$

This is readily derived from Equations (3.1) and (2.5), and subsequent integration by parts leads to the expression :

$$\tilde{\zeta}(k,z,\omega) = -\int_o^d \partial G(k;z,z')/\partial z'\; \tilde{S}(k,z,\omega)/\,(i\omega)\, dz' \tag{3.20}$$

The differentiated sum in G_R of (3.20) has an n^{-3} convergence rate and can be differentiated again, as required for evaluation of the pressure from (2.6a). As may be seen from Equations (2.6), the remaining fields are very simply evaluated from the pressure and displacement fields. In the

evaluation of the pressure, there arises the term

$$\partial^2 G_\infty/\partial z\partial z' = k\cosh(kz_<)\cosh[k(z_>-d)]/\sinh(kd) - \delta(z-z');$$

the delta function removes the isolated $\tilde{S}$ term in (2.6a).

The solutions for the triple Fourier transforms of the various fields can all be expressed in the common form :

$$\tilde{f}(k,z,\omega) = \int_o^d \tilde{S}(k,z',\omega)\, K_f(k,\omega;z,z')\, dz', \tag{3.21}$$

where f denotes any one of the six fields. The various kernels are

$$\left.\begin{matrix} K_\zeta(k,\omega;z,z') \\ K_w(k,\omega;z,z') \end{matrix}\right\} = M_1(k,c;z,z') \times \begin{cases} i/\omega, & (3.22a) \\ -1, & (3.22b) \end{cases}$$

$$\left.\begin{matrix} K_p(k,\omega;z,z') \\ K_u(k,\omega;z,z') \\ K_v(k,\omega;z,z') \end{matrix}\right\} = M_2(k,c;z,z') \times \begin{cases} i\omega\rho_o/k^2, & (3.22c) \\ ik_x/k^2, \quad \text{and} & (3.22d) \\ ik_y/k^2. & (3.22e) \end{cases}$$

Auxiliary function M_1 is just $\partial G/\partial z'$ and M_2 is the regular part of the second mixed derivative $\partial^2 G/\partial z\partial z'$; i.e. with the δ-function arising from differentiation of G_∞ as noted above excluded. Function M_1 has the explicit expression

$$M_1(k,c;z,z') = \sum_{n=1}^{\infty} \Gamma_n(k;z,z')\, c_n^4(k) \,/\, [c_n^2(k) - c^2] \; + \Gamma_o(k;z,z') \tag{3.23a}$$

where

$$\Gamma_n(k;z,z') \equiv \vec{\phi}_n(k,z)\, \vec{\phi}_n'(k,z'), \tag{3.23b}$$

and

$$\Gamma_o(k;z,z') \equiv \begin{Bmatrix} \sinh(kz)\cosh[k(z'-d)] \\ \cosh(kz')\sinh[k(z-d)] \end{Bmatrix} / \sinh(kd). \begin{matrix} (z<z') \\ (z>z') \end{matrix} \tag{3.23c}$$

Similarly, M_2 is given by

$$M_2(k,c;z,z') = \sum_{n=1}^{\infty} \Gamma'_n(k;z,z')\, c_n^4(k) \,/\, [c_n^2(k) - c^2] \;+\; \Gamma'_o(k;z,z') \tag{3.24a}$$

where

$$\Gamma'_n(k;z,z') \equiv \bar{\phi}'_n(k,z)\, \bar{\phi}'_n(k,z'), \tag{3.24b}$$

and

$$\Gamma'_o(k;z,z') \equiv k \cosh(kz) \cosh[k(z'-d)] \,/\, \sinh(kd). \tag{3.24c}$$

Equations (3.21) through (3.24) represent the general transform space solutions for the various fields of interest. These equations could be used for fully time-dependent computations involving arbitrary source distributions undergoing arbitrary motions under the linear and Boussinesq approximations, and are given for future reference purposes. Later, they will be specialized somewhat for the purposes of this report.

4. UNIFORMLY TRANSLATING SOURCE; FREQUENCY INVERSION

At this point, the model is specialized to forcing by a distribution of fluid volume sources over some finite planar region at depth z_s, in uniform common translation at speed c_o parallel to the x-axis, moving in the direction of increasing x and "switched on" at time t=0. Thus the source function has the form

$$S(x,z,t) = \delta(z-z_s)\, S_o(x-c_o t,y)\, H(t), \tag{4.1}$$

where $c_o>0$. It should be noted that several such sources can be readily accommodated by superposition of the individual solutions. In a refined scheme, more general vertical source distributions could be incorporated by retaining the integration over the Green's function, but this will not be considered here. The triple transform of the special source (4.1) is

$$\tilde{S}(k,z,\omega) = -\, i\, \hat{S}_o(k)\, \delta(z-z_s) \,/\, (\omega-c_o k_x), \quad \mathrm{Im}[\omega-c_o k_x] < 0, \tag{4.2a}$$

where

$$\hat{S}_o(k) \equiv (2\pi)^{-1} \iint_{-\infty}^{\infty} S_o(x)\, \exp(ik\cdot x)\, d^2x \tag{4.2b}$$

is a double spatial Fourier transform. The general expression (3.21) immediately simplifies to

$$\tilde{f}(k,z,\omega) = -i\, \hat{S}_o(k)\, K_f(k,\omega;z,z_s) \,/\, (\omega-c_o k_x). \tag{4.3}$$

Recovery of the solutions in the physical domain then involves inversion of the general expression (3.21) according to (2.4b). For the uniformly translating source, it proves convenient to transform to coordinates $x_1 \equiv x + c_o t\, \hat{x}$ moving with the source. The physical-space

solutions then have the general form

$$f(x_1,z,t) = \frac{1}{2\pi} \iint_{-\infty}^{\infty} \hat{S}_o(k)\, L_f(k,t;z,z_s)\, e^{-ik\cdot x}\, d^2k, \qquad (4.4a)$$

where

$$L_f(k,t;z,z_s) \equiv \frac{1}{2\pi i} \int_{-\infty-i\varepsilon}^{\infty-i\varepsilon} K_f(k,\omega;z,z_s)\, \frac{\exp\, i(\omega-c_o k_x)t}{\omega - c_o k_x}\, d\omega. \qquad (4.4b)$$

The first step is evaluation of the frequency inversion integral (4.4b) for the five kernels (3.22). With the special choice (4.2a) of source, it proves possible to evaluate these integrals using residue theory. The source term introduces a simple pole at $\omega=c_o k_x$. The displacement (3.22a) contains an additional pole at $\omega=0$. Moreover, all field transforms have poles where $\omega^2 = k^2 c_n^2$, as is evident from Equations (3.23a) and (3.3). At this point k is real, and so k^2 is merely a positive parameter as far as ω inversion is concerned. Standard[16] Sturm-Liouville theory then shows that the eigenvalues c_n^{-2} are real and therefore that the frequency poles $\pm kc_n$ are on the real ω-axis. There are no other poles in the ω-plane. All eigenfunctions are independent of ω. Thus all poles are simple and appear explicitly as denominator factors of the form $(\omega\pm\omega_p)$. The frequency inversion contour passes below the real axis and so all fields vanish for $t<0$ as may be seen by closing the inversion contour in the lower half plane. For $t>0$, the contour may be closed up, thereby picking up contributions from the poles on the real axis. Evaluation by residue theory is simple if tedious, and leads to the following results.

(a) **Particle displacement:**

$$L_\zeta(k,t;z,z_s) = i\, \Gamma_o(k;z,z_s)\, \Psi(\omega_o,t) - i \sum_{n=1}^{\infty} c_n^2(k)\, \Gamma_n(k;z,z_s)\, \{[\Psi(\omega_n^-,t)+\Psi(\omega_n^+,t)]/2 - \Psi(\omega_o,t)\} \qquad (4.5a)$$

(b) **Vertical velocity:**

$$L_w(k,t;z,z_s) = -\Gamma_o(k;z,z_s) + \sum_{n=1}^{\infty} k\, c_n^3(k)\, \Gamma_n(k;z,z_s)\, [\Psi(\omega_n^-,t)-\Psi(\omega_n^+,t)]/2 \tag{4.5b}$$

(c) **Pressure:**

$$L_p(k,t;z,z_s) = i\omega_o\rho_o(z)\Gamma_o'(k;z,z_s)/k^2 - i\rho_o(z) \sum_{n=1}^{\infty} c_n^4(k)\, \Gamma_n'(k;z,z_s)\, [\Psi(\omega_n^-,t)+\Psi(\omega_n^+,t)]/2 \tag{4.5c}$$

(d) **Horizontal velocity:**

$$L_u(k,t;z,z_s) = i\,\hat{k}\,\Gamma_o'(k;z,z_s)\,/\,k - i\,\hat{k} \sum_{n=1}^{\infty} c_n^3(k)\, \Gamma_n'(k;z,z_s)\, [\Psi(\omega_n^-,t)-\Psi(\omega_n^+,t)]\,/\,2 \tag{4.5d}$$

In these equations, note the auxiliary definitions

$$\omega_o \equiv c_o k_x, \qquad \omega_n^{\pm} \equiv \omega_o \pm \omega_n, \tag{4.6a,b}$$

where

$$\omega_n \equiv k\, c_n(k), \tag{4.7}$$

and

$$\Psi(\alpha,t) \equiv [1-\exp(-i\alpha t)]/\alpha. \tag{4.8}$$

Also, (4.5d) is a vector form, and $\hat{k}$ is a unit vector. Equations (4.4) and (4.5) give the solutions in physical space for all time for the particular source (4.1), and can, in principal, be used to compute the time-evolution of the linearized fluid-dynamical fields, i.e. including transient effects.

5. EXTRACTION OF STEADY-STATE FIELDS

Of greater interest for present purposes is the ultimate steady-state situation viewed in the (uniformly translating) source reference frame. Specifically, the steady-state form f^{∞} for field f is defined by way of

$$f^{\infty}(x,y,z) \equiv \lim_{t\to\infty} f(x_1,y,z,t) = \lim_{t\to\infty} f(x+c_o t,y,z,t) \tag{5.1}$$

It should be noted that for finite $t>0$, the various integrands of Equations (4.5) are well-defined, for $\Psi(\alpha,t)$ is an entire function of both arguments. As $t\to\infty$, the increasingly oscillatory nature of the exponential part in each term $\Psi[\omega_p(k),t]$, at all k-points near which $\omega_p(k)\neq 0$, effectively removes these contributions from the integral (e.g. Riemann-Lebesgue lemma), thereby replacing each such term Ψ by $\omega_p^{-1}(k)$ near such points. However, k-points near real roots k_o of $\omega_p(k)=0$ present problems. These lead to poles in the resulting steady-state integrands on the respective axes of integration. The attendant ambiguities can be circumvented as follows[8]. Near such points the ensemble of integration may be shifted into the respective complex planes, (i.e. $k_o+\delta k$, δk complex) for any finite t due to the analyticity of the integrands. On the displaced contour near such a zero,

$$\Psi[\omega_p(k),t] \simeq [1-\exp(-it\Lambda)]/\Lambda \tag{5.2a}$$

where

$$\Lambda \equiv \delta k\cdot\nabla_k\, \omega_p(k_o). \tag{5.2b}$$

This deformation is then to be done in such a way that $\mathrm{Im}[\Lambda]<0$ everywhere on the deformed portions; the corresponding exponential term of Ψ decays in time, and the resulting term Λ^{-1} is non-singular on the deformed contour in the steady-state limit. If there are points k_o on the real axes at which also $\nabla_k\,\omega_p = 0$, a higher approximation must be used; this possibility will be considered further later.The relevant ω_p are given in (4.6), and have k-gradients:

$$\nabla_k \omega_o = (c_o, 0) \; ; \tag{5.3a}$$

$$\begin{aligned} \nabla_k \omega_n^{\pm} &= \left(c_o \pm k_x c_{gn}(k)/k, \; \pm k_y \, c_{gn}(k) \, / \, k \right) \\ &= \left([c_o^2 - c_n(k_o) c_{gn}(k_o)]/c_o, \; \pm k_{oy} c_{gn}(k_o) \, / \, k_o \right). \end{aligned} \tag{5.3b}$$

The final expression on the right-hand side is evaluated at the appropriate k_o, and the horizontal group speed is defined as

$$c_{gn}(k) \equiv d\omega_n(k)/dk. \tag{5.3c}$$

It will be shown later that $|c_{gn}| < |c_n| < |c_o|$ for poles on the real k_x-axis, so that $(c_o^2 - c_n c_{gn})_o \geq 0$. The possibility of equality is ignored here for now, and only the k_x-contour is deformed, leaving k_y as a real parameter in the complex k_x-integrals. The deformation criterion (comment following (5.2b)) is then satisfied by deforming the k_x-contour below each resulting steady state pole on the real k_x-axis.

The resulting expressions for the steady-state physical fields can be written in the general form

$$f^{\infty}(x,z) = (2\pi)^{-1} \int_{-\infty}^{\infty} \left\{ \int_{K_{-\infty}}^{\infty} \hat{S}_o(k) \, L_f^{\infty}(k,z) \, e^{-ix \cdot k} \, dk_x \right\} dk_y \tag{5.4}$$

Here the k_y-integral is confined to the real axis, and the k_x-integral is taken along a contour K initially consisting of the real k_x-axis, indented below any real poles. With dependence of the various ω_p and Γ on their respective arguments (k) and $(k; z, z_s)$ suppressed in the notation, the kernels have the expressions :

(a) **Particle displacement:**

$$L_{\zeta}^{\infty}(k,z) = i\Gamma_o/\omega_o \; - \; i \sum_{n=1}^{\infty} \Gamma_n \, k^2 \, c_n^4(k) \, / \, [\, \omega_o (\, \omega_o^2 - \omega_n^2 \,) \,]. \tag{5.5a}$$

(b) **Vertical velocity:**

$$L_w^\infty(k,z) = -\Gamma_o + k \sum_{n=1}^{\infty} \Gamma_n k^2 c_n^4(k) / (\omega_o^2 - \omega_n^2). \tag{5.5b}$$

(c) **Pressure:**

$$L_p^\infty(k,z) = i\omega_o\rho_o\Gamma_o'/k^2 - i\rho_o\omega_o \sum_{n=1}^{\infty} \Gamma_n' c_n^4(k) / (\omega_o^2 - \omega_n^2). \tag{5.5c}$$

(d) **Horizontal velocity:**

$$L_u^\infty(k,z) = i \hat{k} \Gamma_o'/ k - i\hat{k} \sum_{n=1}^{\infty} \Gamma_n' k c_n^4(k) / (\omega_o^2 - \omega_n^2). \tag{5.5d}$$

Note that in the infinite sums for w, p and u_h, the respective convergence rates in n, for each fixed **k** in the integrands, are $O(n^{-3})$, $O(n^{-2})$, $O(n^{-3})$. The ω_o term in the infinite sum for the displacement field, which may be isolated by a partial fraction expansion of the denominator, is independent of n, and by (3.17) this isolated term could be evaluated explicitly to cancel the Γ_o term outside the sum. However the remaining infinite sum would have only $O(n^{-1})$ convergence, in contrast to the $O(n^{-3})$ behaviour of (5.5a).

Finally, note from (5.5c) and (5.5d) that $L_p^\infty = c_o \rho_o(z) L_u^\infty$; these expressions are essentially partial fraction expansions of the respective fields, and the numerators have the same values at the poles ω_o, $\omega_n^\pm$. Thus the steady-state pressure is proportional to the x-velocity component at any depth. This may also be seen from the dynamical equations upon transformation to coordinates translating with the source and looking for solutions independent of time. The pressure field will therefore be excluded from further consideration.

6. EVALUATION OF k_x-INTEGRALS

(a) Preliminaries

As in the case of the frequency integrals earlier, the k_x-integrals (5.4) arising in computation of the steady state fields are amenable to evaluation by residue theory.

There are poles due to zeros of the sinh(kd) ($k\neq 0$) terms in the denominators of Γ_o and Γ'_o. There are also poles at $k_x=0$ in the displacement, and a pole at $k=0$ (and therefore at $k_x = \pm i|k_y|$)in the horizontal velocity fields. These poles give rise to near-field disturbances and are independent of the N^2-profile details. Finally, there are poles where $\omega_n^2 = \omega_o^2$, which depend on the details of the profile and represent the radiating internal wave wake.

The coefficient Q of ζ in the differential equation (2.5a) is $[N^2(z)/c^2-k^2]$. This coefficient must be positive somewhere on (0,d) in order that the solution not be of a purely exponential nature. Thus it is evident that for $k^2\to\infty$, $c_n^2\to 0+$. It has already been seen (in the discussion for G^∞) that if $|c_n^2|\to\infty$, then $k^2\to (n\pi/d)^2$. Moreover, when $k^2<0$, the d.e. is always oscillatory for $c^2>0$, and also for certain values of $c^2<0$. This leads to the basic rules that $(k^2>0) \Rightarrow (c^2>0)$, and conversely $(c^2<0) \Rightarrow (k^2<0)$. The basic behaviour of the eigenvalue curves $c^2 = c_n^2(k)$ in the (c^2,k^2) plane is sketched in Figure 1 (lighter curves with negative slope). These curves were computed for a constant-N ocean, and are included purely for illustrative purposes.

The poles $\omega_n^2 = \omega_o^2$ can be located as follows. These must satisfy the dual constraints $c^2 = c_o^2k_x^2/k^2$ (which is a restatement of the equation $\omega^2 = \omega_o^2$) and $c^2 = c_n^2$ (i.e. they must be eigenvalues). For a fixed k_y, the first constraint is equivalent to a hyperbola

$$(c_o^2-c^2)k^2 = c_o^2k_y^2 \qquad (6.1)$$

in the (c^2,k^2) plane. A sample of such a hyperbola is also sketched as the darker curve (positive slope) in Figure 1. The intersections of the

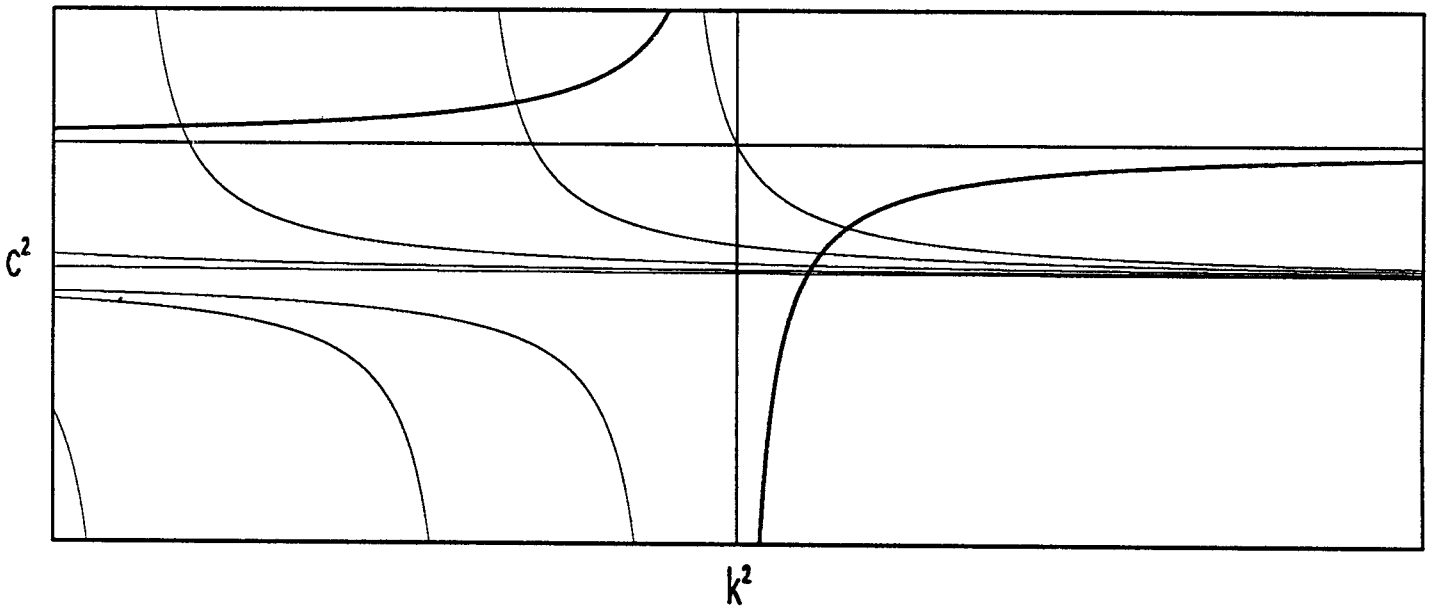

Figure 1. Sample dependence of five eigencurves c_n^2 on k^2 is shown by the lighter curves. The darker curve depicts a constraint hyperbola of the form $(c_o^2-c^2)k^2 = c_o^2k_y^2$.

hyperbola with the eigenvalue curves give two discrete families of poles satisfying the constraint, one with $k^2>0$ and the other with $k^2<0$. Both families have a horizontal asymptote $c^2=c_o^2$. Poles with $k^2>0$ have $0<c^2<c_o^2$, whereas those with $k^2<0$ have $c^2>c_o^2$. In both cases $c^2>0$, so that $k^2>0$ corresponds to $k_x^2>0$, i.e. to poles on the real k_x-axis. Similarly, the poles with $k^2<0$ correspond to poles on the imaginary k_x-axis.

In order to evaluate the k_x-integral via contour integration it is necessary to compute the residue at each pole $1/\omega_n^{\pm}$. If these poles are simple, the residue calculation involves the reciprocal of the derivative $d\omega_n^{\pm}/dk_x$, evaluated at the pole. Since the modal frequencies depend on k only

via k^2, it is found that

$$d\omega_n^{\pm}/dk_x = c_o \pm (k_x/\omega_n) d\omega_n^2/dk^2. \tag{6.2a}$$

Evaluation at $\omega_n^{\pm}=0$ gives

$$(d\omega_n^{\pm}/dk_x)_o = [c_o^2 - (d\omega_n^2/dk^2)_o]/c_o, \tag{6.2b}$$

the subscript "o" denoting evaluation at the pole. Note that the term $d\omega_n^2/dk^2$ can also be written as $c_n c_{gn}$ as in (5.3). An integral expression for this term can be obtained as follows. From (3.15) and (3.13) it follows immediately that

$$\int_o^d \dot{Q}(k,c;z)\ \phi_n^2(k,z)\ dz = 0, \tag{6.3}$$

since $\Delta(k,c) = 0$ along any eigencurve. Note that the derivative in (6.3) is total, since there is just one free parameter describing an eigencurve. Let the parameter be k^2, then

$$\int_o^d [N^2/\omega_n^2 - 1 - (k^2N^2/\omega_n^4) d\omega^2/dk^2]\ \phi_n^2\ dz = 0.$$

This is readily rearranged, with the help of normalization definition (3.6a), to

$$d\omega_n^2/dk^2 = c_n^2\ [1 - \omega_n^2 \int_o^d \bar{\phi}_n^2\ dz]. \tag{6.4}$$

The left-hand side of (6.2) may therefore be expressed as

$$(d\omega_n^{\pm}/dk_x)_o = (c_o/k_n^2)[k_y^2 + c_o^2\ k_{xn}^4 \int_o^d \bar{\phi}_n^2\ dz]. \tag{6.5}$$

The term in square brackets is strictly positive for both real and imaginary poles, except if $k_y = 0$, and $k_x=0$ is also a pole. Evidently, for $k_y \neq 0$, the poles in k_x are all simple. Moreover, even if $k_y=0$, the poles are still simple so long as the corresponding value of k_{xo} is non-zero, or if the

limiting value of the ratio k_y/k_n is non-zero. With reference to Figure 1, note that as $k_y \to 0$, the hyperbolic curves degenerate to the lines $k^2=0$, $c^2=c_o^2$. Clearly a double pole is possible in at most one point, and then only if $c_m^2(0) = c_o^2$ for some eigencurve. This situation could be resolved by deforming the k_y-contour near $k_y=0$ also, but this will not be considered further here. Related problems are removed by any realistic source term (see (6.11) below). Note that for poles with $k^2>0$, the right-hand side of (6.4) is then positive, as mentioned in conjunction with (5.3c).

From the definition of the phase speed, Eq.(6.4) can be expressed alternatively as

$$dc_n^2/dk^2 = -c_n^4 \int_o^d \bar{\phi}_n^2 \, dz. \tag{6.6}$$

This shows that each curve c_n^2 is a strictly decreasing function of k^2, a standard[7] result, and is illustrated by the sample curves of Figure 1.

For the real roots ($k_x^2>0$), the constraint $c_o^2k_x^2 = k^2c_n^2$ may be written in polar form by defining $k_x = k\cos\theta$, $k_y = k\sin\theta$. The n^{th} eigencurve is then specified in the form $(k,\theta_n(k))$. The constraint reduces to

$$\cos^2[\theta_n(k)] = c_n^2(k)/c_o^2. \tag{6.7}$$

The right-hand side is a well-defined function of k, and as $k\to\infty$, it approaches 0, and so $\theta_n \to \pm\pi/2$; the curves have a vertical asymptote. If it happens that $c_n^2(0) < c_o^2$, then the curve passes through the origin in the (k_x,k_y)-plane, at angle $\theta_n(0)$. Such curves are termed super-Froude[6] and are infinite in number. They contain only diverging waves. Alternatively, if $c_n^2(0)>c_o^2$, then there is some finite value of k at which $\theta_n(0)=0$. The slopes of the curves are given by

$$dk/d\theta = -c_o\sin(\theta)/c_n'. \tag{6.8}$$

This second type of curve is termed sub-Froude and each such curve cuts the k_x-axis with vertical slope as is evident from (6.8) - they give rise to modes containing transverse waves. There are at most a finite number of modes of this type. If the source speed c_o is sufficiently high that $c_o \geq c_1(0)$, then all modes are super-Froude.

Similarly the constraint for the imaginary modes may be rewritten as follows. Define $k_x = ik\cosh\mu$, $k_y = k\sinh\mu$ where $k \geqq 0$. Then

$$\cosh^2\mu = c_n^2(k)/c_o^2. \tag{6.9}$$

It is readily seen that for any super-Froude mode, the corresponding μ (and consequently k_x) is bounded away from zero. The associated wake contribution thus decays exponentially away from the source with a factor $\exp(-|xk_x(0)|)$. Conversely, any sub-Froude mode has μ-values down to zero and the associated contribution from the k_x-integrals might be expected to decay only algebraically with distance from the source.

(b) Source notes

The source (4.1) is represented by a horizontally bounded distribution S_o of sources on the plane $z=z_s$. Let these sources lie between x_{min} and x_{max}. Then in general, the Fourier transform $\hat{S}_o$ will possess exponential growth for $|Im(k_x)|\to\infty$. Closure of the various k_x-contours will thus be possible only for $x > x_{max}$ and $x < x_{min}$. Thus the result of this contour deformation will describe the far-field propagating internal wavefield, and the near-field both ahead of and behind the extremes of the source distribution. Computations for $x_{min} < x < x_{max}$ would require alternative computational methods, and will not be considered further here.

Since the source distribution S_o is real, its transform (4.2b) satisfies the property

$$[\hat{S}(\mathbf{k})]^* = \hat{S}(-\mathbf{k}^*), \tag{6.10}$$

the asterisk denoting complex conjugation.

A realistic source model must conserve mass. This requires that the integral of $\nabla\cdot\mathbf{u}$ taken over a volume completely enclosing the source distribution S must vanish. For the source (4.1), this requirement reduces to $\iint_{-\infty}^{\infty} S_o(\mathbf{x})\, d^2\mathbf{x} = 0$, which is equivalent to

$$\hat{S}(0) = 0. \tag{6.11}$$

This constraint will be assumed in what follows. It alleviates potential singular behaviour near $\mathbf{k}=0$.

(c) Evaluation of the integrals

It has been seen above that the n^{th} term of each infinite sum in Equations (5.5) contains two real and two imaginary poles in k_x. Denote these as

$$\pm\mu_n(k_y),\ \pm i\nu_n(k_y), \tag{6.12}$$

where μ_n, $\nu_n \geq 0$ by definition. As noted earlier, there are additional poles at zeros of sinh(kd) ($k \neq 0$). These lie at $k^2 = -n^2\pi^2/d^2 \equiv -\gamma_n^2$, and so in the k_x-plane at

$$k_x^2 = -\delta_n^2(k_y) \equiv -\left(k_y^2 + \gamma_n^2 \right), \tag{6.13}$$

where by definition, $\delta_n \geq 0$. Thus there are poles at $k_x = \pm i\delta_n(k_y)$. The plus (minus) sign thus refers to poles in the upper (lower) half k_x-plane. Finally there is a pole at $k_x=0$ in the displacement integral, and poles at $k_x = \pm i|k_y|$ in the horizontal velocity integrals.

The details of the residue calculation then form a standard but tedious exercise in algebra. The final results, which represent the working equations for a computational scheme, are presented below. With reference to Equation (5.4), it is evident that all fields can be expressed in the form of a single inverse Fourier transform in k_y.

$$f^{\infty}(x,z) = \int_{-\infty}^{\infty} \bar{f}(x,k_y,z)\, \exp(-iyk_y)\, dk_y, \tag{6.14a}$$

where

$$\bar{f}(x,k_y,z) \equiv (2\pi)^{-1} \int_{K_{-\infty}}^{\infty} \hat{S}_o(k_x,k_y)\, L_f^{\infty}(k_x,k_y,z)\, e^{-ixk_x}\, dk_x. \tag{6.14b}$$

The results of evaluation of the k_x-integral (6.14b) by residue theory (closing up if $x<x_{min}$ and down if $x>x_{max}$ as necessitated by an above note) may be summarized as :

$$\bar{f}(x,k_y,z) = \sum_{n=0}^{\infty} H_{fn}(k_y,z,z_s)\, a_f^+\, \hat{S}_o(-i\delta_n,k_y)\, \exp(-x\delta_n) \; - \; \sum_{n=1}^{\infty} I_{fn}(k_y,z,z_s)\, a_f^+\, \hat{S}_o(-i\nu_n,k_y)\, \exp(-x\nu_n)$$

$$(\; x > x_{max} \;) \tag{6.15a}$$

$$\bar{f}(x,k_y,z) = D_f(k_y,z,z_s)\,\hat{S}_o(0,k_y) +$$

$$\sum_{n=0}^{\infty} H_{fn}(k_y,z,z_s)\,a_f^-\,\hat{S}_o(+i\delta_n,k_y)\,\exp(+x\delta_n) -$$

$$\sum_{n=1}^{\infty} \Big\{ I_{fn}(k_y,z,z_s)\,a_f^-\,\hat{S}_o(+i\nu_n,k_y)\,\exp(+x\nu_n) +$$

$$R_{fn}(k_y,z,z_s)\big[\, b_f^+\,\hat{S}_o(+\mu_n,k_y)\,\exp(-ix\mu_n) +$$

$$b_f^-\,\hat{S}_o(-\mu_n,k_y)\,\exp(+ix\mu_n)\,\big] +$$

$$E_{fn}(k_y,z,z_s)\,\hat{S}_o(0,k_y)\,\Big\}.$$

$$(\, x < x_{min}\,) \qquad (6.15b)$$

In these equations the a's and b's are constants defined by

$$a_u^{\pm} = \pm 1,\ a_v^{\pm} = +i,\ a_w^{\pm} = +1,\ a_\zeta^{\pm} = \pm 1, \quad \text{and} \qquad (6.16a)$$

$$b_u^{\pm} = +1,\ b_v^{\pm} = \pm 1,\ b_w^{\pm} = \pm i,\ b_\zeta^{\pm} = +1. \qquad (6.16b)$$

The coefficients H (Hyperbolic, for want of a better identifying term) arise from the poles in the sinh(kd) term, and are defined by

$$\left.\begin{aligned} H_{un}(k_y,z,z_s) &\equiv 1 \qquad (6.17a)\\ H_{vn}(k_y,z,z_s) &\equiv k_y/\delta_n \qquad (6.17b)\end{aligned}\right\} \varepsilon_n \cos(\gamma_n z)\cos(\gamma_n z_s)\,/\,d,$$

and

$$\left.\begin{aligned} H_{wn}(k_y,z,z_s) &\equiv 1 \qquad (6.17c)\\ H_{\zeta n}(k_y,z,z_s) &\equiv 1/(c_o\delta_n) \qquad (6.17d)\end{aligned}\right\} \gamma_n \sin(\gamma_n z)\cos(\gamma_n z_s)\,/\,(\delta_n d).$$

In these expressions,

$$\varepsilon_n \equiv (1/2,1)\ (n=0,n>0). \qquad (6.17e)$$

The coefficients I arising from the poles on the imaginary k_x-axis, and R arising from poles on the real axis, due to the terms $\omega_n^{\pm}$ of (5.5), share the common functional form

$$\left.\begin{aligned} G_{un}(k_y,z,z_s) &\equiv 1 \\ G_{vn}(k_y,z,z_s) &\equiv k_y/|k_{xn}| \end{aligned}\right\} \times \frac{c_n^4\, \Gamma_n'(k;z,z_s)}{2(c_o^2 - d\omega_n^2/dk^2)}\,, \qquad \begin{aligned} &(6.18a)\\ &(6.18b)\end{aligned}$$

and

$$\left.\begin{aligned} G_{wn}(k_y,z,z_s) &\equiv |k|c_n \\ G_{\zeta n}(k_y,z,z_s) &\equiv 1 \end{aligned}\right\} \times \frac{c_o c_n^2\, \Gamma_n(k;z,z_s)}{2(c_o^2 - d\omega_n^2/dk^2)}\,. \qquad \begin{aligned} &(6.18c)\\ &(6.18d)\end{aligned}$$

These are to be evaluated with

$$k_x = +i\nu_n(k_y), \quad k = +i(\nu_n^2 - k_y^2)^{1/2}, \qquad (G = I\ ), \tag{6.19a}$$

and

$$k_x = +\mu_n(k_y), \quad k = +(\mu_n^2 + k_y^2)^{1/2}, \qquad (G = R\ ). \tag{6.19b}$$

Note the suppressed dependence of c_n etc. on k in the notation. The remaining terms E_{fn} and D_f are zero for all but the displacement field,

$$E_{un} = E_{vn} = E_{wn} = 0 \tag{6.20a}$$

$$D_u = D_v = D_w = 0 \tag{6.21a}$$

$$E_{\zeta n}(k_y,z,z_s) \equiv -\,\Gamma_n(|k_y|,z,z_s)\; c_n^2(|k_y|) \;/\; c_o \tag{6.20b}$$

$$D_{\zeta}(k_y,z,z_s) \equiv -\,\Gamma_o(|k_y|,z,z_s) \;/\; c_o \tag{6.21b}$$

The coefficients (6.16) through (6.17) have all been constructed so as to be real. The above Equations (6.14) through (6.21) represent the main working results for numerical computation of the fields. The next section will consider the details of numerical evaluation of the various terms in these equations.

The above results hold for an arbitrary source distribution $S_o(x)$ subject to condition (6.11). If the source has symmetry properties, the above results simplify considerably. In particular, let it be assumed that the source distribution is symmetric in y and antisymmetric in x, i.e.

$$S_o(-x,y) = -S_o(x,y), \quad S_o(x,-y) = S_o(x,y).$$

This property transfers to the Fourier transform $\hat{S}_o(k_x,k_y)$, i.e. it also is antisymmetric with respect to its first argument and symmetric with respect to its second. It then follows that if α and k_y are both real, then so are both of $\hat{S}_o(i\alpha,k_y)$ and $-i\hat{S}_o(\alpha,k_y)$. Under this simplifying assumption, the above solutions may be put in the common form :

$$\bar{f} = A_{fo}(x) \left\{ \sum_{n=o}^{\infty} H_{fn}\, C_{hn}\, \exp(-|x\delta_n|) + \sum_{n=1}^{\infty} I_{fn}\, C_{in}\, \exp(-|x\nu_n|) \right\}$$
$$+ H(-x) \sum_{n=1}^{\infty} 2\, R_{fn}\, C_{rn}\, A_{fn}(x). \tag{6.22}$$

In this expression, explicit dependence on k_y, z, z_s, etc., has been suppressed in an obvious manner. The expression is valid if $x>x_{max}$ or if $x<x_{min}$. The first pair of terms are present both ahead of and behind the source, and represent a localized or near-field disturbance. The leading A functions are defined by

$$A_{fo}(x) \equiv [-1,\ -\mathrm{sgn}(x),\ -1,\ -i\,\mathrm{sgn}(x)\ ],\ f=[\zeta,w,u,v]. \tag{6.23}$$

The third term is present only downstream of the source and represents the internal wave wake generated by the source. Functions A_{fn} are defined by

$$A_{fn}(x) \equiv \{\ \sin,\ \cos,\ -\sin,\ i\cos\}[x\mu_n(k_y)],\quad f=[\zeta,w,u,v]. \tag{6.24}$$

The terms C are related to the source function by :

$$C_{hn} \equiv \hat{S}_o[i\delta_n(k_y),k_y], \quad C_{in} \equiv \hat{S}_o[i\nu_n(k_y),k_y], \quad \text{and}$$

$$C_{rn} \equiv -i\ \hat{S}_o[\mu_n(k_y),k_y], \tag{6.25}$$

and are real on account of the above note. Thus the above expression(6.22) is real and even in k_y for the field components u,w,ζ, and is imaginary and odd in k_y for field v.

7. NUMERICAL CONSIDERATIONS

(a) Preliminaries

Computation of a physical field component is based on Equations (6.14) through (6.21). The integration over k_y is implemented efficiently using well-known Fast Fourier Transform (FFT) methods. This is a major reason for evaluation of the k_x-integrals by complex variable methods, leaving k_y as a real parameter, and it essentially allows simultaneous computation of many cross-track points at each fixed x and z.

The heart of the problem is therefore the computation of the eigenvalues, eigenfunctions and various coefficients in order to do the modal summations of (6.15b) at any fixed set of values $\{x,k_y,z,z_s,c_o\}$ with a given N^2 profile.

(b) Differential Equation Solution; General

The next step is computation of values of the Wronskian Δ in order to find zeros. This entails solution of the homogeneous differential equation (3.4a), together with boundary conditions (3.8), for a given profile. With dependence on the parameters suppressed for now, the differential equation can be written as a first-order linear system,

$$\boldsymbol{\Phi}'(z) = \underline{\mathbf{A}}(z)\ \boldsymbol{\Phi}(z), \tag{7.1a}$$

where

$$\boldsymbol{\Phi} = \begin{bmatrix} \phi \\ \phi' \end{bmatrix}, \qquad \underline{\mathbf{A}} = \begin{bmatrix} 0 & 1 \\ -Q(z) & 0 \end{bmatrix} \tag{7.1b}$$

(Note the convention that uppercase bold Greek symbols denote 2×1 column vectors, and uppercase bold underlined Roman symbols denote 2×2 matrices.) The solution to (7.1a) can always be expressed in the form

$$\boldsymbol{\Phi}(z) = \underline{\mathbf{F}}(z,z_o)\ \boldsymbol{\Phi}(z_o) \tag{7.2}$$

Here, $\underline{F}$ is a fundamental matrix[16] ("propagator") relative to z_o, which satisfies initial conditions $\underline{F}(z_o,z_o)=\underline{I}_2$ (the 2×2 identity matrix) and whose columns each satisfy (7.1a). Note the basic results

$$\underline{F}(z,z_o) = \underline{F}^{-1}(z_o,z), \tag{7.3a}$$

$$\underline{F}(z,z_1) = \underline{F}(z,z_o)\ \underline{F}(z_o,z_1). \tag{7.3b}$$

The determinant of $\underline{F}$ is independent of z since $\underline{A}$ has zero trace, and the initial conditions show that

$$\det(\underline{F}) = 1. \tag{7.3c}$$

It follows from Equations (3.8),(3.10), (7.1) and (7.2) that the Wronskian Δ has the expression

$$\Delta = \underline{F}_{12}(z,0)\underline{F}_{22}(z,d) - \underline{F}_{22}(z,0)\underline{F}_{12}(z,d), \tag{7.4a}$$

where the subscripts refer to matrix components. The left-hand side is independent of z, and so the right-hand side can be evaluated at any convenient reference depth $0\leq z\leq d$.

If it should prove necessary to evaluate derivatives of the Wronskian with respect to some parameter, two approaches are possible. If the derivatives of $\underline{F}$ are available analytically, then (7.4a) may be differentiated directly :

$$\begin{aligned}\dot{\Delta} = {} & \dot{F}_{12}(z,0)\ F_{22}(z,d) + F_{22}(z,0)\ \dot{F}_{12}(z,d) \\ & - \dot{F}_{22}(z,0)\ F_{12}(z,d) - F_{22}(z,0)\ \dot{F}_{12}(z,d).\end{aligned} \tag{7.4b}$$

The other approach is to differentiate (3.10) directly, and obtain the

eigenfunction derivatives by solution of the augmented matrix differential system

$$\begin{bmatrix} \phi \\ \phi' \\ \dot{\phi} \\ \dot{\phi}' \end{bmatrix}' = \begin{bmatrix} 0 & 1 & 0 & 0 \\ -Q & 0 & 0 & 0 \\ 0 & 1 & 0 & 0 \\ -\dot{Q} & 0 & -Q & 0 \end{bmatrix} \begin{bmatrix} \phi \\ \phi' \\ \dot{\phi} \\ \dot{\phi}' \end{bmatrix}, \tag{7.5}$$

subject to the appropriate boundary conditions derived from (3.8).

(c) Layered Profile

Numerical values for the profile N^2 will generally be obtained from measured data and defined on a discrete mesh of points. Many methods can be employed for solution of the differential equation.

One possible approach is a three-point finite difference scheme[18,19,20]. This method leads to a tridiagonal matrix eigenvalue problem, which has the advantage of approximating the eigenvalues of the differential equation as those of an n^{th}-order matrix. Although the matrix elements are extremely simple, an excessively fine mesh may be needed to adequately resolve portions of the eigenfunctions with large vertical wavenumbers.

Another possible approach is to use piecewise approximations to the profile which allow the differential equation to be solved analytically. For example, piecewise linear approximations lead[21] to Airy function solutions which may be used to construct the fundamental matrices $\underline{F}$ in the various segments. While such methods provide accurate solutions on a realistic approximation to the physical profile there may be the added burden of computation of the various higher transcendental functions which arise.

The approach to be used here is to use the simplest possible approximation to the profile, namely "layers" within which N^2 is piecewise constant. This so-called multilayer[17,22] or Thomson-Haskell[23] approach leads to eigenfunctions which are piecewise trigonometric or hyperbolic elementary

functions. This approach is suitable[24] for the present problem since the basic profile data is N^2 and this does not appear in differentiated form in the differential equation. With proper treatment, these solutions can be suitably stabilized as explained below. Note that this approximation may be more properly thought of as suitably joined local WKB approximations to the eigenfunctions for the true profile, rather than a stepped approximation to the true profile. The phase of the local trigonometric solutions allows more efficient eigenfunction approximation in regions of large vertical wavenumber than finite difference methods.

Thus for a given profile, a set of points $\{z_o=0<z_1<\ldots<z_n=d\}$ is introduced, giving n layers, of which the m^{th} has constant value N_m and thickness $h_m \equiv z_m - z_{m-1}$. An example of a such profile is shown in Figure 2. It is based on measured[12] summertime temperature/salinity data taken at Ocean Station P. From this data, N^2-values were computed, and 31 layers fitted to a smoothed version. The plot displays N(z) in units of cycles per hour as a function of depth in metres. The profile shows a pronounced pair of maxima. Only the top 1250m of data is plotted; the actual profile extends to a depth d=4133m, with N=0 below the plotted values.

The solution form (7.2) for any points z and z_o within the same layer may then be written as

$$\Phi(z) = \underline{I}[Q_m^{1/2}; z-z_o]\ \Phi(z_o), \tag{7.6}$$

where the fundamental or propagator matrix $\underline{I}$ is defined by

$$\underline{I}(\alpha,h) \equiv \begin{bmatrix} \cos(\alpha h) & \sin(\alpha h)/\alpha \\ -\alpha \sin(\alpha h) & \cos(\alpha h) \end{bmatrix}. \tag{7.7}$$

If this propagator is for a whole layer, it is denoted $\underline{I}_m$, i.e.

$$\underline{I}_m \equiv \underline{I}(\alpha_m, h_m). \tag{7.8}$$

Note that α may be imaginary.

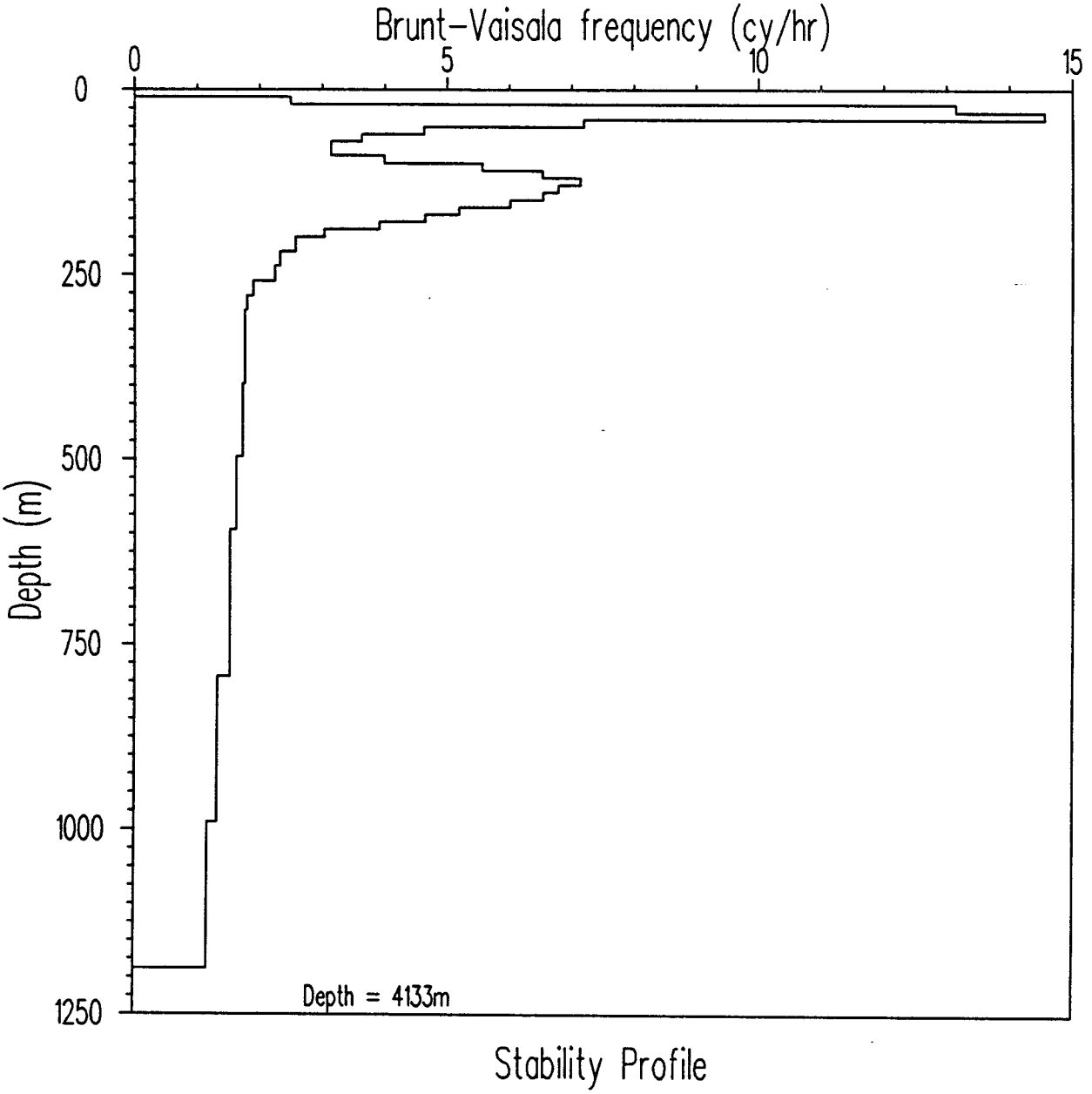

Figure 2. The layered Brunt-Vaisala frequency profile used for the examples in this report. It is based on a smoothed version of measured data taken at Ocean Station P during the summertime.

In this multilayer Boussinesq approximation, appropriate conditions on the solution are continuity of ϕ and ϕ' for $0<z<d$ (this is because the differential equation contains no derivatives of N^2). Thus by application of the general form (7.3b) or simple iteration of (7.6), it is readily seen that if z_r is within layer 'm', then

$$\Phi_o(z_r) = \underline{T}[\alpha_m; z_r - z_m]\underline{T}_{m-1}\cdots\underline{T}_1\Phi_o(0), \tag{7.9a}$$

and

$$\Phi_d(z_r) = \underline{T}[\alpha_m; z_r - z_{m+1}]\underline{T}_{m+1}^{-1}\cdots\underline{T}_n^{-1}\Phi_d(d). \tag{7.9a}$$

The left-hand sides contain the information necessary for evaluation of the Wronskian Δ at an intermediate depth z_r. In principal, this reference depth may be chosen at either boundary, and so the Wronskian can be expressed as

$$\Delta = \underline{P}_{12}, \tag{7.10a}$$

where the matrix $\underline{P}$ represents the fundamental matrix relative to z=0, evaluated at z=d, i.e.

$$\underline{P} \equiv \underline{T}_n\underline{T}_{n-1}\cdots\underline{T}_1. \tag{7.10b}$$

This is in fact the first equality of (3.10a) in the present notation.

(d) Auxiliary Variables

For numerical purposes it proves convenient to work in terms of new parameters (p,s) in place of (k^2,c^2). These are defined by

$$p \equiv \omega^2/N_{max}^2, \qquad s \equiv N_{max}^2/c^2 \tag{7.11}$$

A convenient combination is the special value

$$s_c \equiv N_{max}^2/c_o^2, \tag{7.12}$$

which is related to the Froude number[4], but has the dimensions of reciprocal length squared. The equations inverse to (7.11) express (k,c) in terms of (p,s),

$$k^2 = sp, \qquad c^2 = N_{max}^2/s \tag{7.13}$$

The coefficient Q of the differential equation (3.4) then becomes

$$Q(p,s;z) = s[\nu(z)-p], \tag{7.14}$$

where ν is a dimensionless profile

$$\nu(z) \equiv N^2(z)/N_{max}^2, \quad (\ 0 \leq \nu \leq 1 \ ). \tag{7.15}$$

The physical eigenvalues of the modified form of (3.4) then define a set of monotonically increasing curves $s_m(p)$ in the (p,s) plane, confined to $-\infty<p<1$, $s\geq 0$.

Portions of the first 21 eigencurves $s_n(p)$ in Quadrant I of the (p,s)-plane are shown in Figure 3. These correspond to the profile shown in Figure 2, and are displayed in a log-log (base 10) format in order to separate the various curves better. Note that numbers on the axes give the actual values of p and s, not their logarithms.

The main interest is in those points which lie on these eigencurves and also satisfy either of the constraints $\omega^2 = c_o^2 \, k_x^2$ in the case of coefficients (6.18), or $k_x^2 = 0$ in the case of (6.20b). In terms of the new parameters, the first constraint translates to

$$(s-s_c)p = k_y^2, \tag{7.16a}$$

and the second to

$$sp = k_y^2. \tag{7.16b}$$

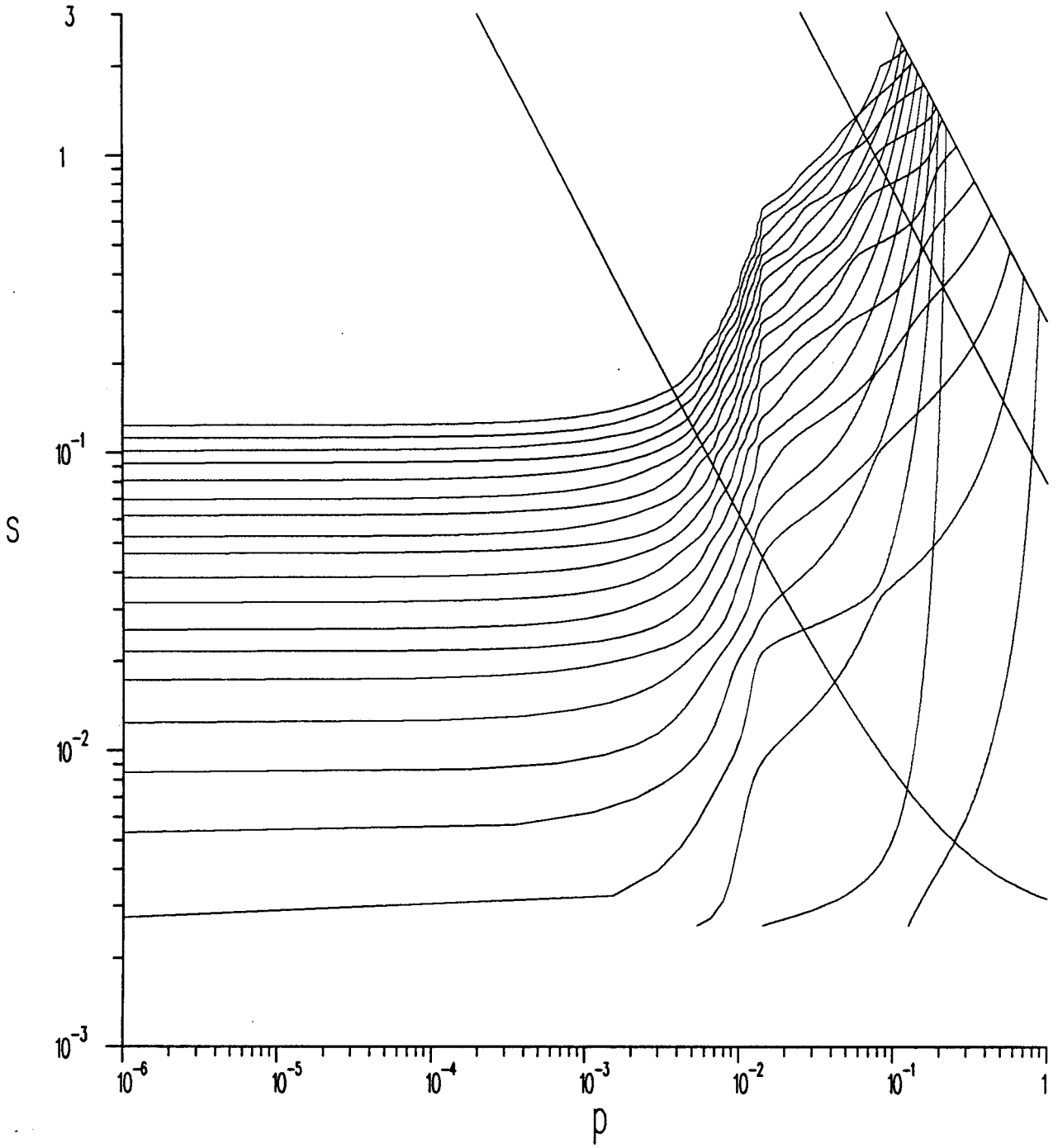

Figure 3. Portions of the first 21 eigencurves in Quadrant I of the (p,s) parameter plane for the profile of Figure 2. Although the various curves approach each other with exponentially small separation at a discrete number of points, they do not intersect each other. The illusion of two sets of curves is due to the presence of the two peaks in the profile, as discussed in the text. Also shown are three constraint curves along which eigenvalues are sought for a fixed value of k_y and source speed.

Both represent hyperbolae in the (p,s)-plane, and have the s-axis as a vertical asymptote. The second constraint hyperbola intersects the eigenvalue curves only in the first quadrant $p,s \geq 0$, providing a denumerable infinity of intersections $\{p_m, s_m\}$ corresponding to real eigenvalues. The first constraint has a horizontal asymptote in $s>0$, and so provides a first denumerable set of solutions $\{p_m^-, s_m^-\}$ in the second quadrant $s \geq 0, p \leq 0$ corresponding to the imaginary eigenvalues of (6.19a), and a second set $\{p_m^+, s_m^+\}$ in the first quadrant $s \geq 0, p \geq 0$ corresponding to the real eigenvalues of (6.19b). The effect of a increase in source speed c_o is to shift the horizontal asymptote in (7.16a) downwards, while the effect of an increase in k_y is to increase the distance of the hyperbolae from the origin. The eigencurves themselves are a property purely of the N^2-profile. The imposition of the c_o and k_y values merely dictates how these curves are "sampled" in the integrations leading to the physical fields.

For each fixed k_y (to be dictated by the integration scheme chosen for the ultimate integration of (6.14a)), the finding of eigenvalues is thus conveniently reduced to a one-dimensional problem of searching along the hyperbolae (7.16), which can be expressed in terms of a single suitable variable. Hyperbola (7.16a), for example, may be described by a parameter 'v' by way of the definitions

$$p(v) = \sigma(v) - v/2; \quad s(v) = s_c + \sigma(v) + v/2 \quad \text{(Quadrant I)}, \tag{7.17a}$$

$$p(v) = -\sigma(v) - v/2; \quad s(v) = s_c - \sigma(v) + v/2 \quad \text{(Quadrant II)}, \tag{7.17b}$$

where

$$\sigma(v) \equiv \left(k_y^2 + v^2/4 \right)^{1/2}, \quad \text{and} \quad -\infty < v < \infty; \tag{7.18}$$

the signs in (7.17) have been chosen so as to make $s'(v)>0$, $p'(v)<0$ on both arms of the hyperbola. Hyperbola (7.16b) may be parametrized by equations analogous to (7.17) with s_c replaced by 0.

Sample hyperbolae of the form (7.17) for several k_y-values are also shown on Figure 3. In the log-log form used, these hyperbolae become

almost linear; $\log(p) + \log(s-s_c) = 2\log(k_y)$. The speed used for these constraint illustrations was $c_o=0.5$ ms^{-1}, and the k_y-values correspond to $\{j(\pi/3072)$ rad m^{-1}; j= 25, 271, 513 $\}$. The intersections of any one of these hyperbolae with the eigencurves give the corresponding set of modal points $\{p_m^+, s_m^+\}$ described above, for the value of k_y under consideration.

Thus once c_o and k_y are fixed, the constrained eigenvalue problem has only the single parameter v, and involves finding zeros of the (real) function

$$D(v) \equiv \Delta[p(v),s(v)] \quad (-\infty<v<\infty), \tag{7.19}$$

where Δ is the Wronskian (3.9), expressed in terms of the new parameters. Figure 4 shows plots of D(v) along the three constraint hyperbolae plotted of Figure 3. Note that the v-ranges on each plot are different; the parametrization (7.17) varies with k_y.

(e) Effects of Interior Evanescent Regions

In practice, the presence of evanescent layers (imaginary vertical wavenumbers $Q_m<0$), for certain values of the parameters (p,s), is a well-known source of difficulty[11,25,26]. As may be seen from (7.14), the differential equation coefficient for the m^{th} layer is $Q_m=s(\nu_m-p)$. As noted above, the imaginary eigenvalues have $-\infty<p\leq 0$, $s>0$ and so all layers are oscillatory. However the real eigenvalues have $s>0$ and $0\leq p\leq 1$. Thus for a given value of p, all layers with $\nu_m<p$ will be evanescent. If not properly handled, these regions may cause numerical exponential overflows and inappropriate approximations for eigenfunctions. Moreover, such regions may cause eigenvalues to be exponentially close together and so cause multiple eigenvalues in a numerical implementation. Such multiplicities and overflows must be handled carefully, but this can be done in a straightforward manner as will be explained later. Before a general discussion however, it is instructive to consider a symmetric three-layer profile.

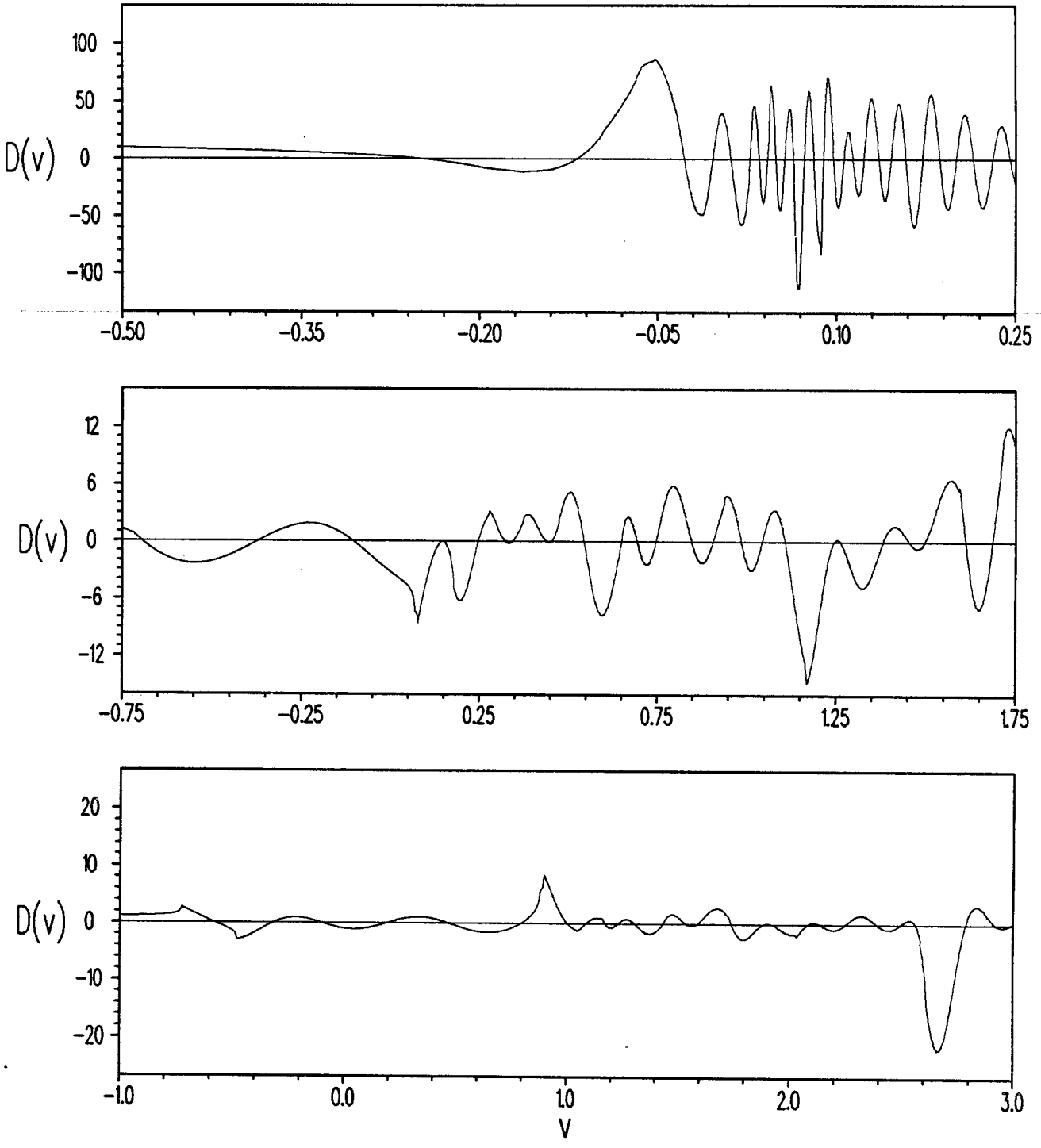

Figure 4. Plots of the scaled Wronskian D(v) along the three cuts depicted on Figure 3. The three values of k_y chosen increase down the page. Note that the close separation of the fourth and fifth zeros in the central plot causes their apparent coalescence into a double zero.

(f) A Symmetric Three-layer Example

The symmetric three-layer profile is shown in Figure 5.

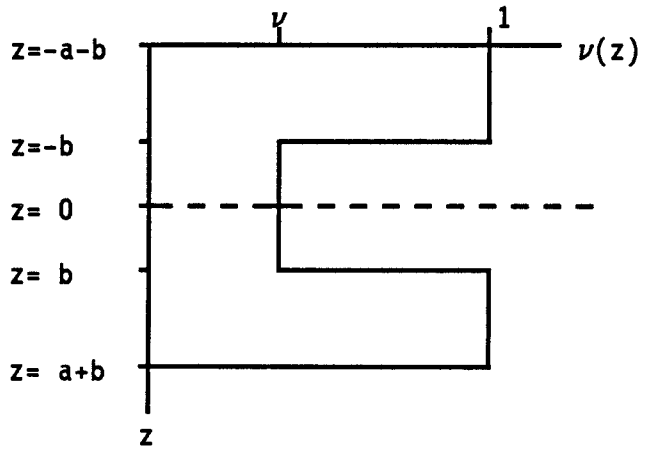

Figure 5. Symmetric three-layer profile. Note that the origin has been shifted for purposes of this discussion.

It is convenient for purposes of discussion to consider the surface to be at z=-a-b and the bottom at z=a+b. Thus the centre layer has thickness '2b', and the differential equation coefficient there is $\beta^2 \equiv s(\nu-p)$. The two flanking layers each have thickness 'a' and coefficient $\alpha^2 \equiv s(1-p)$. Within the centre region the general solution necessarily has the form

$$\phi(z) = A\cos(\beta z) + B\sin(\beta z)/\beta.$$

It may then be shown that

$$\phi(\pm a \pm b) = LA \pm MB,$$

where

$$L \equiv \cos(\beta b)\cos(\alpha a) - (\beta/\alpha)\sin(\beta b)\sin(\alpha a),$$

$$M \equiv \sin(\beta b)\cos(\alpha a)/\beta + \cos(\beta b)\sin(\alpha a)/\alpha.$$

The boundary conditions $\phi(\pm a \pm b) = 0$ then result in the homogeneous equations:

$$LA+MB=0, \quad LA-MB=0,$$

so that either

$$L=0, \quad B=0 \text{ (even eigenfunctions)},$$

or

$$M=0, \quad A=0 \text{ (odd eigenfunctions)}.$$

In terms of the standard notation, it may be shown that for this problem

$$\Delta = 2LM,$$

i.e. the Wronskian factors into a product of two terms. The eigenvalue conditions are thus

$$\alpha\cot(\alpha a) = \beta\tan(\beta b) \text{ (even)},$$

or

$$\alpha\cot(\alpha a) = -\beta\cot(\beta b) \quad \text{(odd)}.$$

If the eigenfunctions are normalized to unit slope at the upper ($z=-a-b$) boundary, so that they correspond to the "upper" solutions ϕ_o of the standard notation, they may be written in the form:

$$\phi_E = \begin{cases} \dfrac{\sin[\alpha(a+b+z)]}{\alpha} \\ \dfrac{\sin(\alpha a)}{\alpha}\dfrac{\cos(\beta z)}{\cos(\beta b)}, \\ \dfrac{\sin[\alpha(a+b-z)]}{\alpha} \end{cases} \qquad \phi_O = \begin{cases} \dfrac{\sin[\alpha(a+b+z)]}{\alpha} & -b-a<z<-b, \\ -\dfrac{\sin(\alpha a)}{\alpha}\dfrac{\sin(\beta z)}{\sin(\beta b)}, & -b<z<b, \\ -\dfrac{\sin[\alpha(a+b-z)]}{\alpha} & b<z<a+b, \end{cases}$$

where the subscripts here denote Even or Odd eigenfunctions respectively. If $\nu<p<1$, then the centre layer is evanescent, and $\beta=i|\beta|$. The outer layers

are oscillatory, and the Wronskian Δ may be written as:

$$\Delta = [\sinh(2|\beta|b)\sin(\alpha a)/(\alpha|\beta|)] \times$$
$$[\alpha\cot(\alpha a)+|\beta|\coth(|\beta|b)]\,[\alpha\cot(\alpha a)+|\beta|\tanh(|\beta|b)].$$

The above eigenvalue conditions reduce to

$$\alpha\cot(\alpha a) = -|\beta|\tanh(|\beta|b) \quad \text{(even)},$$

or

$$\alpha\cot(\alpha a) = -|\beta|\coth(|\beta|b) \quad \text{(odd)}.$$

If the product $|\beta|b$ is large, two points may be noted. Firstly, the leading $\sinh(2|\beta|b)$ causes the Wronskian Δ to become exponentially large except near its zeros. Secondly, both the $\tanh(|\beta|b)$ and $\coth(|\beta|b)$ right hand sides approach the common value 1, and so the eigenvalues merge into pairs with exponentially small separation. These factors exhibit both the exponential overflow and multiple zero problems mentioned in the preceding section. As will be shown below, the exponential amplitude factor is easily handled, but the presence (in a numerical sense) of multiple zeros may cause problems.

Consider now the eigenfunctions in the presence of this evanescent layer. In this centre layer the even eigenfunctions have the form

$$\phi_E(z) = \alpha^{-1}\sin(\alpha a)\cosh(|\beta|z)/\cosh(|\beta|b),$$

while the odd eigenfunctions have the form

$$\phi_O(z) = -\alpha^{-1}\sin(\alpha a)\sinh(|\beta|z)/\sinh(|\beta|b).$$

For large $|\beta|b$ products, the eigenfunctions in the outer layers corresponding to two closely-separated modes may be numerically indistinguishable, apart from a possible change in sign in one of the oscillatory layers. This may be seen from the above general expressions for the eigenfunctions, where an even and adjacent odd eigenfunction may have

values of α which are exponentially close together. In the evanescent layer, the eigenfunctions are essentially zero over most of the layer. The additional interior zero of the sinh term ensures that in principal it represents the next higher mode, but in practice it may be impossible to distinguish numerically between the exponentially small values of the cosh term and the "true" zero in the sinh term.

The exponential smallness in the interior evanescent layer at first glance appears to represent "tunnelling" of a finite amplitude eigenfunction through a region of extreme smallness, only to reappear with finite amplitude in the other layer. The resolution[27] lies in consideration of the eigenfunction expansion, including the source term. Suppose that the source is in one of the outer oscillatory layers (cf sound channels in acoustics). By grouping the modal summation in pairs over adjacent modes in those terms where the eigenvalues coalesce, it can be seen that the source excites these two modes equally in its own layer, but the sign change of the eigenfunctions in the opposite layer removes any contribution there. Thus for numerical purposes, a modified set of eigenfunctions may be defined by doubling the amplitude in one half of the profile and zeroing it in the other. Thus when an eigenvalue pair is numerically indistinguishable, it is counted twice, and used to form two numerically orthogonal eigenfunctions which are disjoint and normalized over half the profile (which effectively doubles their amplitude in each layer in keeping with the pairwise regrouping in the eigenfunction expansion). It is then the source which dictates which of the disjoint (modified) eigenfunctions is excited. The end result is that energy excited in a given "waveguide" subsection of the overall profile remains confined to that region.

(g) Treatment of Interior Evanescent Regions

Now return to consideration of the more general problem in which there may be multiple interior evanescent regions. The exponential growth problem can be easily circumvented simply by factoring out an exponential term from the matrix for each evanescent layer in the product (7.10).

Specifically, (7.10) may be recast in the form

$$\underline{P} = \underline{Q} \exp[\, \int_o^d \mathrm{Im}\sqrt{Q(z')}\, dz' \,], \tag{7.20a}$$

where

$$\underline{Q} = \underline{R}_n \underline{R}_{n-1} \cdots \underline{R}_1, \tag{7.20b}$$

and

$$\underline{R}_m \equiv \underline{T}_m \exp[-\mathrm{Im}(h_m\sqrt{Q_m})]. \tag{7.20c}$$

If the layer is oscillatory (Q>0) , then the matrix $\underline{R}$ is identical to $\underline{T}$ as defined in (7.7). However, if the layer is evanescent, then $\underline{R}$ has the form

$$\underline{R} = \begin{bmatrix} [1+\exp(-2\alpha h)]/2 & [1-\exp(-2\alpha h)]/(2\alpha) \\ \alpha[1-\exp(-2\alpha h)]/2 & [1+\exp(-2\alpha h)]/2 \end{bmatrix}, \tag{7.21}$$

where here $\alpha \equiv \mathrm{abs}(\mathrm{Im}\sqrt{Q})$. The elements of each matrix $\underline{R}$ are bounded, and for an evanescent layer they are also positive. Moreover, if several adjacent interior layers are evanescent, then the product of the corresponding $\underline{R}$'s is also bounded and has positive elements. There is then no numerical difficulty (or "instability") in evaluation of the matrix product (7.20b).

The above approach is similar to ones used elsewhere[25,28]. Specifically, (discontinuous) amplitude control functions $\chi_{o,d}$ for solutions of the differential equation are defined by way of

$$\chi_o(z) \equiv \exp[\, \int_o^z \mathrm{Im}\sqrt{Q(z')}\, dz' \,], \tag{7.22a}$$

$$\chi_d(z) \equiv \exp[\, \int_z^d \mathrm{Im}\sqrt{Q(z')}\, dz' \,]; \tag{7.22b}$$

the integrands here are by convention either zero or positive. Scaled "eigenfunctions" $\underline{\Psi}_{o,d}$ are then defined by

$$\underline{\Phi}_o(z) \equiv \chi_o(z)\underline{\Psi}_o(z);\ \underline{\Phi}_d(z) \equiv \chi_d(z)\underline{\Psi}_d(z). \tag{7.23a,b}$$

The functions χ limit any exponential growth in the scaled eigenfunctions

away from their respective boundary and the modified functions $\underline{\Psi}$ are bounded.

On account of (7.20a), a zero of $\underline{Q}$ is one of $\underline{P}$, and hence an eigenvalue. The eigenvalue search is then reduced to finding zeros of the (1,2) element of the bounded matrix $\underline{Q}$. It should be noted that extensive numerical experimentation verifies that there is no need to evaluate the Wronskian at an interior reference depth[25] for the purposes of root-finding. However, as will be discussed later, more care is needed with construction of the eigenfunctions, where the evanescent layers may introduce artificial amplification of the eigenfunctions in inappropriate regions of the profile.

It may be noted that for an evanescent layer, $\det(\underline{R}) = \exp(-2\alpha h)$. Thus for evanescent layers with large α-h products, or for a set of adjacent layers whose integrated α-h product is large, the determinant of the corresponding matrix can vanish (underflow) numerically. This feature in effect factors the eigenvalue problem into two subproblems in which an artificial rigid boundary (or appropriate radiation condition) is introduced into the evanescent region. This is the generalization of the exact factorization which arises in the symmetric three-layer model above. Specifically, suppose that the profile contains an interior region of high evanescence. Then the factors of (7.20b) may be regrouped as

$$\underline{Q} = \underline{LEU}, \tag{7.24a}$$

where $\underline{L}$ denotes the product of matrices for all layers from below the evanescent region to the bottom, $\underline{E}$ represents all layers within the evanescent region under consideration, and $\underline{U}$ represents all layers above the evanescent region. (Note that $\underline{L},\underline{U}$ may themselves contain evanescent regions, in which case the present argument is iterated). Numerically, $\det(\underline{E})\simeq 0$, so $\underline{E}_{11}\underline{E}_{22}\simeq\underline{E}_{12}\underline{E}_{21}$. Substitution of this relationship into (7.24a) leads to the result

$$\underline{Q}_{12} \simeq (\underline{LE})_{12}(\underline{EU})_{12}/\underline{E}_{12}. \tag{7.24b}$$

The denominator is strictly positive. The two numerator factors in effect represent separated eigenvalue problems. In the first sub-problem, the "upper" profile (represented by $\underline{U}$) overlies the evanescent region ($\underline{E}$), and in the second, the evanescent region overlies the "lower" structure represented by $\underline{L}$. The separated problems thus correspond to the total propagator matrices $\underline{LE}$ and $\underline{EU}$. Each factor will contain its own zeros, leading to the possibility of multiple zeros in the left hand side of (7.24b), depending on the details of the profile. In general these will occur only at discrete points, where families of eigencurves corresponding to each subsection approach each other exponentially closely and in effect appear to cross.

This effect is clearly visible in Figure 3. It should be emphasized that the eigencurves do not intersect each other - they do however approach each other with exponentially small separation at a discrete number of points. These points of close approach give the illusion of two distinct sets of curves for larger (p,s) values. These pseudo-curves in fact correspond to eigencurves appropriate to the two regions on either side of the interior minimum of the profile of Figure 2, which is evanescent for sufficiently large values of p.

The interference effect of the two factors in (7.24b) is also evident in Figure 4. It is more pronounced for higher values of k_y, when the interior evanescence is higher. The central plot of Figure 4 exhibits two very closely separated zeros corresponding to modes 4 and 5. This is also evident in Figure 3 where the corresponding constraint curve appears to pass through an intersection of the fourth and fifth eigencurves.

The presence of highly evanescent interior regions thus need not cause problems in searching for eigenvalues, but a complete numerical scheme must be able to find and properly interpret multiple roots. Note that a more sophisticated scheme could in effect avoid multiple root-finding by appropriately subsectioning the profile, depending on the range of parameters, and looking for separate families of eigenvalues appropriate to

each section, as defined by (7.24b). These eigenvalues could then be appropriately sorted later. This method would correspond to finding zeros in the separated factors as in (7.24b) when evanescence is significant, but involves additional 'bookkeeping' for the various regions. Note that in terms of the parameters (p,s), the physical eigenvalues all have s>0, so that regions of evanescence are controlled only by the parameter p. A subsectioning approach would then be easiest to implement for problems requiring eigenvalues at fixed values of p (i.e. ω^2). For the moving source problem however, both p and s are constrained to a hyperbola, and so the number and extent of evanescent regions varies with the parameter v, thereby presenting additional complications in implementing a subsectioning scheme of this type. Such an approach was not found necessary for finding eigenvalues in the profiles used to date, however.

(h) Computation of the Eigenfunctions

As noted above, interior evanescent layers may induce numerical multiple zeros for certain values of the parameters (p,s). The problem, and common cause of "instability" in the presence of evanescent regions, comes in computation of the corresponding eigenfunctions.

For example, in the three layer profile above, it will prove difficult to evaluate the "true" eigenfunctions by integration in one direction due to the exponential smallness in the centre region. It is easier to compute the "modified" eigenfunctions described above however, by integrating inward from each boundary to a reference depth in one oscillatory layer, and then repeating the procedure for a second reference depth in the other oscillatory layer.

Thus in the general profile, the presence of interior evanescent regions may cause artificial amplification in construction of eigenfunctions, if the reference depth is not chosen appropriately.

A "standard"[7] N^2 profile has a single peak (thermocline) at some depth. The N^2 tapers to zero toward the mixed surface layers and also toward the bottom. There are no multiple eigenvalues for such a profile, and computation of the eigenfunctions is easily handled[25] by choosing a reference depth z_r in the layer containing the maximum N^2-value. The scaled eigenfunctions Ψ are evaluated from the surface down to z_r and from the bottom up to z_r. These are then suitably matched at $z=z_r$, and finally, the exponential factors (7.22) are included to produce exponential decay through any evanescent layers toward the boundaries.

In the presence of interior evanescent regions, the above procedure must be modified, and the definition of the eigenfunctions modified as was done in the case of the symmetric three-layer profile above. In parameter ranges where the zeros of the Wronskian are well-separated, there is no problem. The matrix product (7.20b) for the current eigenvalue can be split into subproducts over regions separated by evanescent layers according to some prechosen cutoff. (This is easily accomplished by examining $\mathrm{Im}\{Q_m\}$ for each layer.) Specifically, for each group of adjacent interior evanescent layers, a depth z_p may be defined at the "centre of evanescence". Successive such points then decompose the profile into alternating regions, each comprising a central oscillatory section, bounded on each side by an evanescent one. Thus the product $\underline{Q}$ may be symbolically written in the form

$$\underline{Q} \equiv \underline{R}'_1 \, \underline{R}'_2 \, \cdots \, \underline{R}'_M, \tag{7.25a}$$

with each term having the symbolic form

$$\underline{R}' = \underline{EOE}, \tag{7.25b}$$

where the subscripts E and O here indicate evanescent and oscillatory; one of the terms $\underline{E}$ may in fact be the identity matrix near a boundary. One or more of these matrices will have a zero in its (1,2) entry, if the partitioning cutoff is numerically large enough to induce factoring as in (7.24b).

If the zero is a simple one, then a reference depth within the (unique) subsection with an (approximate) zero in its (1,2) entry is chosen. Construction of the eigenfunctions then proceeds as in the case of a single thermocline by integration of the scaled eigenfunctions Ψ to this chosen reference depth. After matching at the reference depth, inclusion of the exponential "tails" represented by the functions χ over the intervals $(0,z_r)$ and (z_r,d) effectively zeros contributions in other regions.

In the case of an eigenvalue of multiplicity 'm', there will be 'm' such regions. The eigenvalue is counted m times, and m (disjoint) eigenfunctions constructed from it by repeating the above procedure for a reference depth chosen once within each of the m regions containing zeros.

The net effect is to produce an eigenfunction which pertains to the subsection in question and has exponentially small (numerically zero) amplitude elsewhere. The procedure thus automatically induces a modified eigenfunction expansion as discussed for the example above, and properly accounts for channelling of energy in interior ducts; it is the source term which selects the appropriate eigenfunction combination.

Figure 6a shows the first, eleventh and twenty-first eigenfunctions over the upper 4000m of the profile of Figure 2. These have been normalized so that $\beta_n^2 = N_{max}^2$ (see Equations (3.6a) and (7.30a)). The corresponding values of k_y and c_o are $(\pi/768)$ rad m^{-1} and 0.5 ms^{-1} respectively. For such a small wave number there are no significant evanescent regions except for the bottom section. These long wavelength components 'see' the entire profile.

The effects of interior evanescence and eigenfunction modifications are considered for modes 4 and 5 near the central k_y value illustrated in Figures 3 and 4. This central $k_{yj} = j\pi/3072$, j=271, corresponds to a pair of very closely separated zeros in the Wronskian D(v). Although it is not apparent from the Figures, the two zeros are in fact easily resolved numerically, yet graphically illustrate the eigenfunction

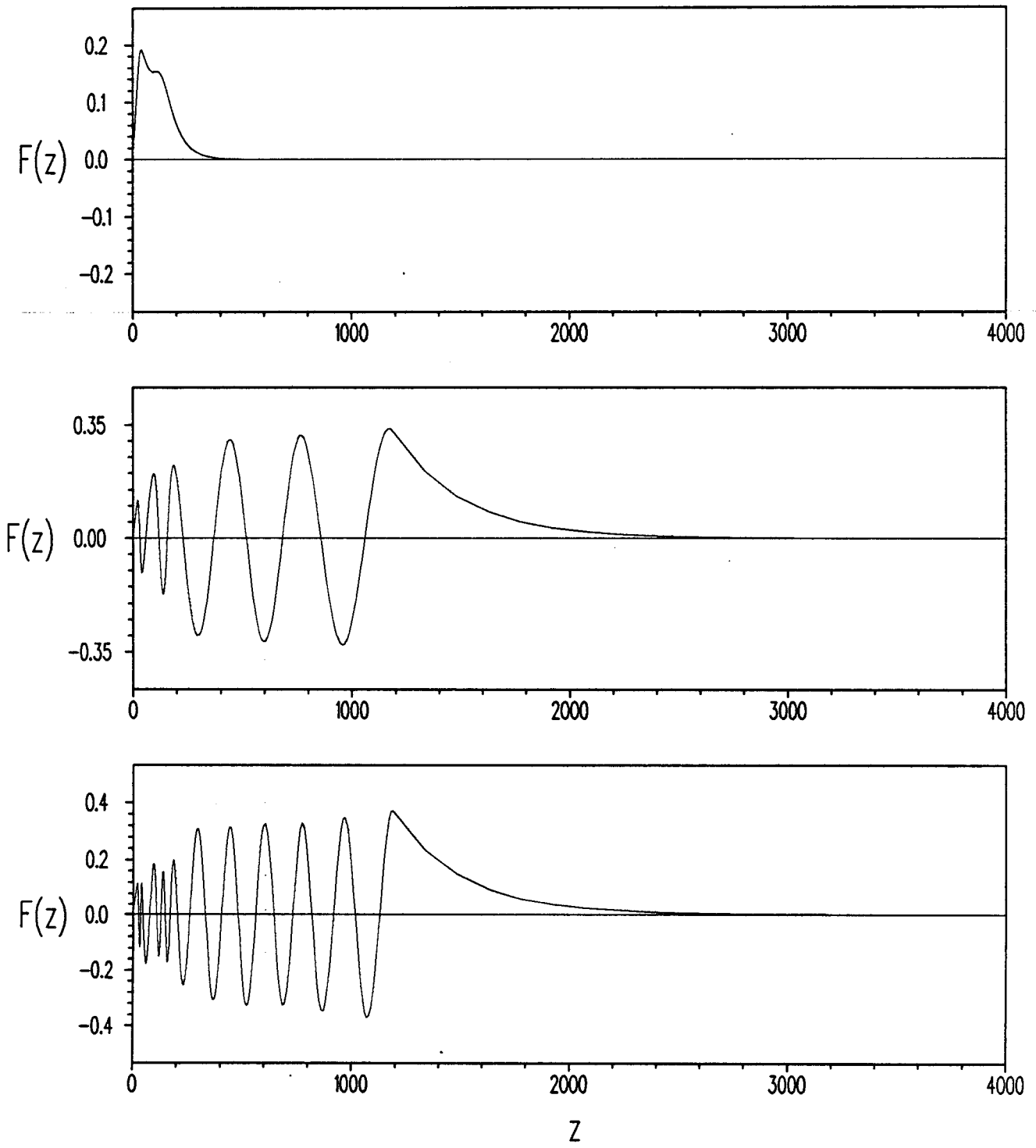

Figure 6a. Normalized eigenfunctions for modes 1, 11 and 21 for a small value of k_y, plotted as a function of depth.

behaviour. Figure 6b shows Mode 4 corresponding to j=269 and j=273, while Figure 6c presents Mode 5 for the same pair of k_y values. The two eigenfunctions exhibit the opposite behaviour in the upper and lower oscillatory sections of the profile.

With reference to Figure 3, it is evident that the point of closest approach of modes 4 and 5 for the full profile corresponds to the first mode of the lower oscillatory subsection of the profile (i.e. the first apparent 'curve' with vertical asymptote near p=0.8), and to the fourth mode of the upper oscillatory region. Thus the eigenfunctions would be expected to have three zeros in the upper section and no zeros in the lower one, as is evident in Figures 6b and 6c.

In Figure 6b, the upper plot is for a k_y-value slightly to the left of the 'intersection' point. As is evident from Figure 3, this corresponds to mode 1 of the lower section, and so is computed for a reference depth there, and decays exponentially toward the boundaries. The lower plot of Figure 6b is for a slightly higher k_y, to the right of the 'intersection' point and so strongly excites mode 4 in the upper section, where the reference depth was chosen.

In Figure 6c, the opposite behaviour is exhibited for mode 5. The only difference is the sign change in the lower section, which is due to an additional zero within the evanescent region, and accounts for this representing mode 5 for the full profile. However, for the purposes of evaluating a fluid dynamical field in which the modes are summed and integrated after inclusion of a source term, it is evident that the 'label' (mode number) applied to a particular mode is of little importance. A source in the lower section, for k_y values near the above 'intersection' point, excites mode 1 of the lower section, regardless of the fact that this is labelled either mode 4 or mode 5 for the full profile for adjacent k_y's.

For purposes of illustration, Figure 6d shows both modes 4 and 5 plotted together for the above pair of k_y values. Due to the exponential

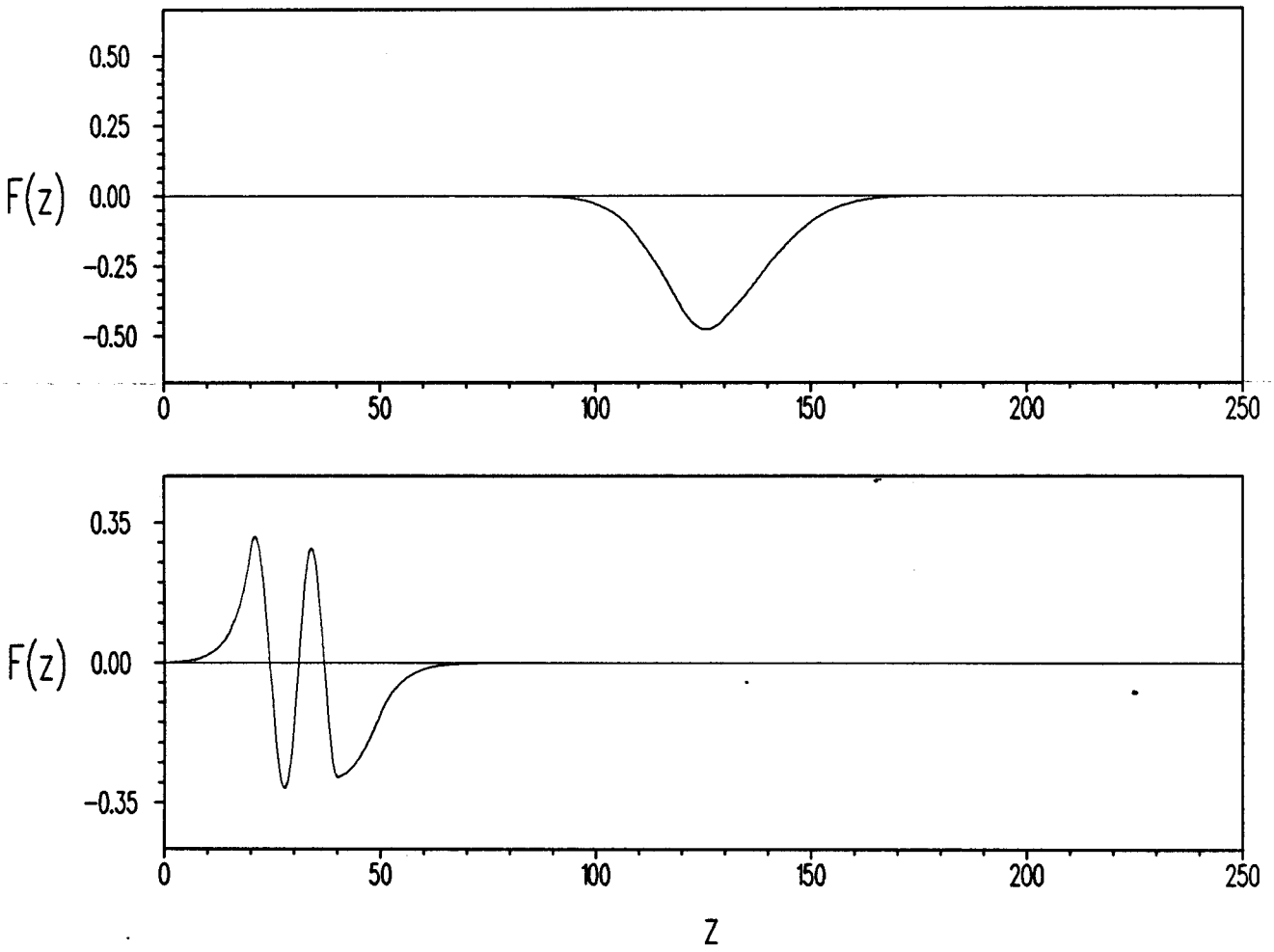

Figure 6b. Normalized eigenfunction for mode 4, for two closely separated intermediate values of k_y, one on either side of the central constraint curve shown on Figure 3. The presence of interior evanescence causes the sudden behaviour change. For the upper value, the eigenfunction looks like mode 1 appropriate to the lower section of the profile in isolation. For the lower plot, it looks like mode 4 appropriate to the upper section. This behaviour can be expected from Figure 3.

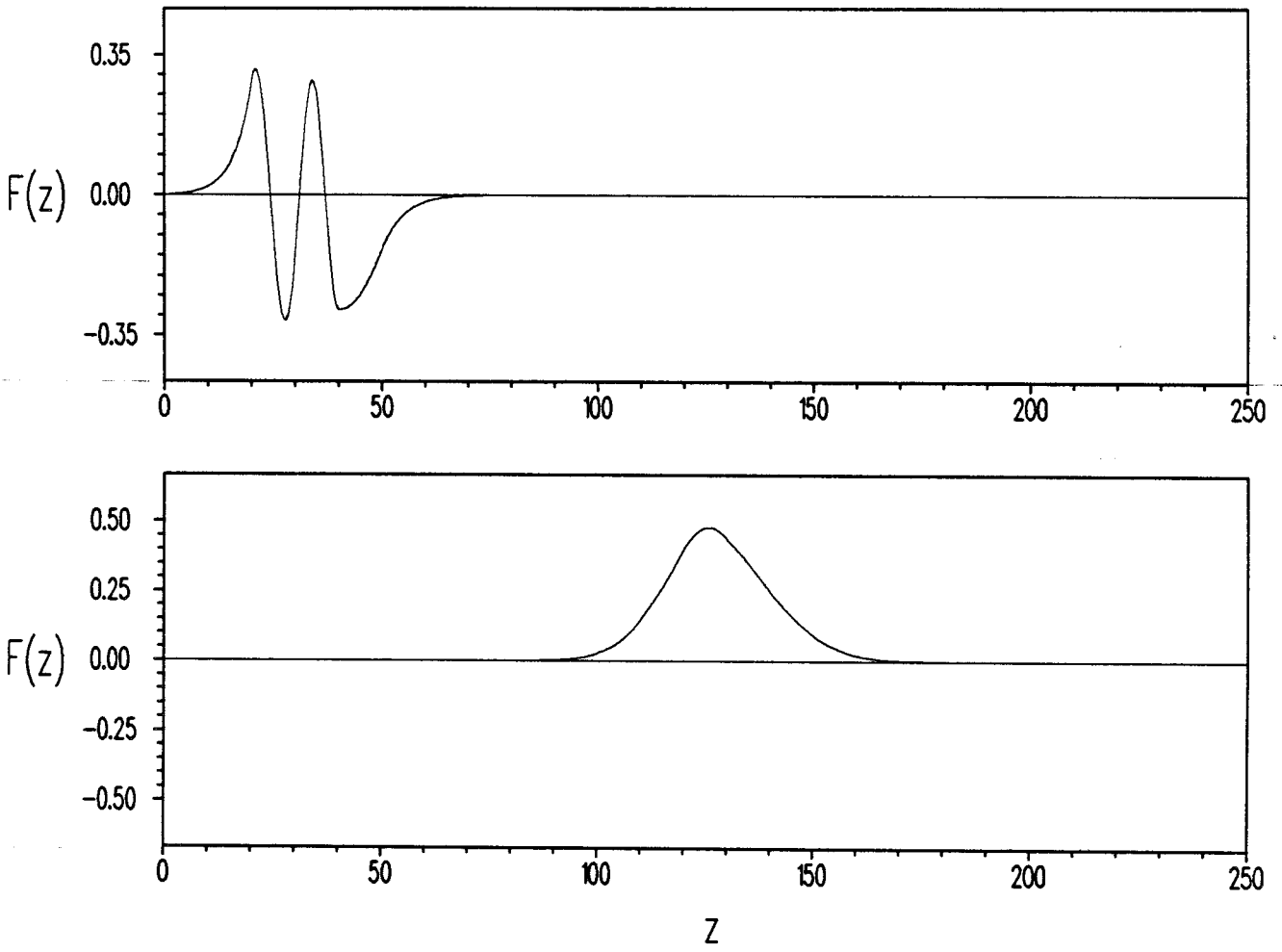

Figure 6c. As in Figure 6b, but for mode 5 of the full profile. The behaviour is reversed for the two k_y values.

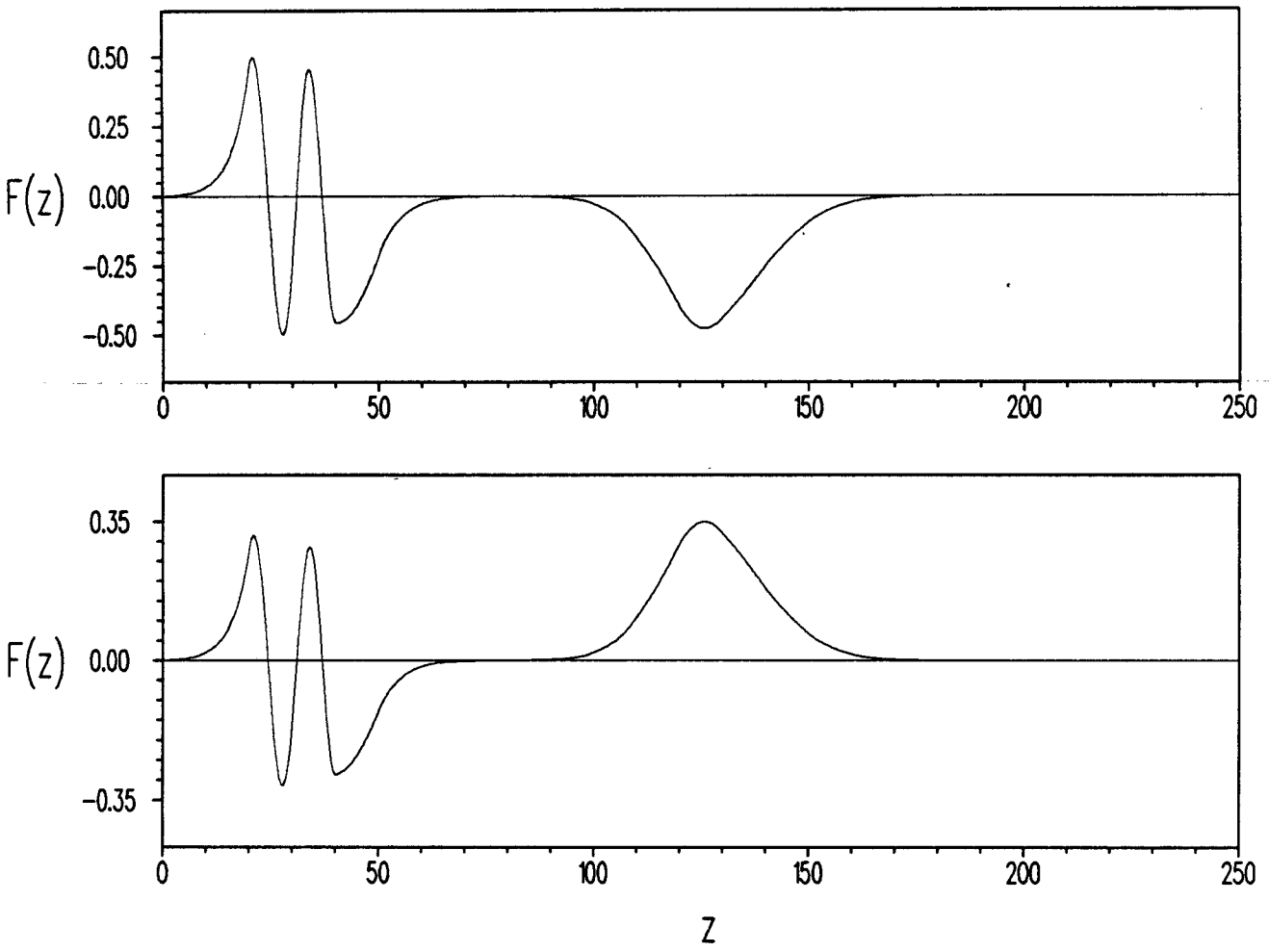

Figure 6d. Figures 6b and 6c plotted together to illustrate the possibility of ambiguity or instability in a standard shooting method for eigenfunction computation. Both the eigenfunction and its derivative are exponentially small in the interior region, and curves looking like any one of the 6 plots of Figures 6b through 6d may be acceptable numerical solutions near closely separated eigenvalues.

smallness of the eigenfunctions in either the upper or lower sections of the profile, these two curves are approximately what is obtained from the sum and difference of modes 4 and 5 near the intersection point. If the evanescence were sufficiently large for the eigenvalue to be a double one in

a numerical sense, then a pair of eigenfunctions looking like the upper and lower curves of Figure 6d would be an acceptable solutions, the upper one connected by a cosh term and the lower one by a sinh term in the evanescent region, precisely as occurred for the symmetric three-layer example above. For numerical purposes however, it preferable to work with the modified forms of Figures 6b and 6c.

(i) Connection with Global Matrix Methods

There is a close connection between the "propagator" approach for solving the differential equation stepwise, and "global matrix" methods[11]. Specifically, if ϕ_i denotes the amplitude of a solution of the differential equation at the i^{th} interface (i=0...n), then it may be shown from the propagator equations (by eliminating the interface derivative values ϕ') that the interface values satisfy the three-term recurrence relation:

$$a_i\,\phi_{i-1} + (b_i+b_{i+1})\,\phi_i + a_{i+1}\,\phi_{i+1} = 0, \tag{7.26a}$$

where

$$a_i \equiv q_i/\sin(q_i h_i), \tag{7.26b}$$

$$b_i \equiv +q_i\cos(q_i h_i)/\sin(q_i h_i), \tag{7.26c}$$

and

$$q_i \equiv Q_i^{1/2}. \tag{7.26d}$$

Together with the boundary conditions $\phi_o = \phi_n = 0$, the above is equivalent to a homogeneous tridiagonal $(n-1)\times(n-1)$ matrix system:

$$\begin{bmatrix} b_1+b_2 & a_2 & 0 & 0 & 0 & \cdots & \\ a_2 & b_2+b_3 & a_3 & 0 & 0 & & \\ 0 & a_3 & b_3+b_4 & a_4 & 0 & & \\ 0 & 0 & & \ddots & & & \\ \vdots & & & & & & \\ & & & & a_{n-1} & b_{n-1}+b_n \end{bmatrix} \begin{bmatrix} y_1 \\ y_2 \\ y_3 \\ \vdots \\ y_{n-1} \end{bmatrix} = \begin{bmatrix} 0 \\ 0 \\ 0 \\ \vdots \\ 0 \end{bmatrix}, \tag{7.27a}$$

which may be written concisely in matrix form as

$$\underline{C}\cdot y = 0, \tag{7.27b}$$

where the matrix/vector notation here refers to dimension n-1. For a non-trivial solution $\det(\underline{C})=0$. In the presence of an interior highly evanescent layer, one of the a's in (7.27a) will be exponentially small and so may be numerically zero in a computer implementation. In this case, the system (7.27b) may be written in partitioned matrix form as:

$$\begin{bmatrix} \underline{C}_1 & \underline{0} \\ \underline{0} & \underline{C}_2 \end{bmatrix} \begin{bmatrix} y_1 \\ y_2 \end{bmatrix} = \begin{bmatrix} 0 \\ 0 \end{bmatrix}. \tag{7.28}$$

In this case, there is again a factorization in the eigenvalue criterion, since

$$\det(\underline{C}) = \det(\underline{C}_1)\ \det(\underline{C}_2). \tag{7.29}$$

The coupling between the pairs in the partition is absent. If $\det(\underline{C}_1)=0$, then a numerically acceptable solution to (7.29) has the form $(y_1,0)$, and similarly if $\det(\underline{C}_2)=0$ a solution has the form $(0,y_2)$. In the case of a coincident pair of eigenvalues, the interpretation is once again a pair of disjoint eigenfunctions $\{(y_1,0),(0,y_2)\}$, the selection of which is again made by the source term. An alternative pair of acceptable solutions is any pair of linearly independent linear combinations of the above pair, and in particular the sum and difference, namely $\{(y_1,\pm y_2)\}$.

(j) Integrands for the Fields

The preceding discussion has explained how eigenpairs (p_m, s_m) may be computed for a specified set of k_y values, and how a corresponding set of (possibly unnormalized) eigenfunctions may be computed in the modified sense described above. The next step is construction of the various terms needed for evaluation of the fields, as given by Equations (6.14a) and (6.15) through (6.21).

The normalization factors (3.6a) are most easily computed directly from the definition by integration:

$$\beta_m^2 = N_{max}^2 \int_o^d \nu(z)\phi_m^2(z)\, dz. \qquad (7.30a)$$

The integration here is done by breaking it into a sum over individual layers and integrating the various terms (which are simple trigonometric or hyperbolic functions) analytically. It is also easy to evaluate the related integrals

$$\varepsilon_m^2 = \int_o^d \phi_m^2(z)\, dz \qquad (7.30b)$$

simultaneously. The slopes $s_m'(p)>0$ of the eigencurves may be expressed in terms of these integrals. Repetition of the calculations which lead to (6.4), in terms of the new parameters (p,s), leads to the equation

$$\int_o^d [\, s_m'(p)\,(\nu-p) - p s_m(p)\,]\,\phi_m^2\, dz = 0,$$

from which it is seen that

$$s_m'(p) = s_m\, \varepsilon_m^2 \,/\, [\beta_m^2 - p\, \varepsilon_m^2\,]. \qquad (7.31)$$

The phase velocities and horizontal total wavenumbers follow from (7.13)

$$k^2 = sp,\ c^2 = N_{max}^2 \,/\, s \qquad (7.32)$$

Values of k_x are either zero or are obtained from

$$k_x^2 = ps_c, \tag{7.33}$$

depending on the field integrand under consideration. Values of k_x and k will be imaginary for p<0. The other quantity of interest is the derivative (6.4), which in the present variables translates to

$$d\omega_m^2/dk^2 = N_{max}^2 \ / \ [s_m(p) + p\ s_m'(p)\ ]. \tag{7.34}$$

With these results, and a description of the source transform $\hat{S}_o$, all of the terms in the integrands (6.15) may be computed.

Figure 7 shows the first 21 real eigenvalues $k_{xm}(k_y)$, corresponding to (7.33). These correspond to the singular curves in the (k_x,k_y) plane, which were of concern in evaluation of the inverse Fourier transform (5.4). These curves are again for the profile of Figure 2, but with a source speed of $2.5ms^{-1}$. For larger k-values, there are again clearly two families of curves, which give the illusion of intersection, corresponding to the two peaks in the profile. For each N^2 maximum taken in isolation, real frequencies would be limited to $\omega^2 < N_{max}^2$, and so $k_x^2 < N_{max}^2/c_o^2$. For the upper peak, N_{max}/c_o=0.01rad/m, while for the lower peak, the corresponding value is 0.005rad/m. The two families of curves clearly display asymptotic approach to these values. All curves pass through the origin; for this profile and source speed, all modes are super-Froude.

The phase velocities corresponding to these same modal curves are shown in Figure 8. All phase speeds are less than the source speed, and show a monotonic decrease both with mode- and wave-number in accordance with known results[7]. Figure 9 contains plots of the ratios $k_{xm}(k_y)/k_y$ as a function of k_y. For this combination, it is evident that all ratios approach a non-zero limit as k_y approaches zero. These real eigenvalues correspond to the radiating internal wave system. The above limiting ratios are related to the angles of propagation of the longest horizontal wavelengths of each

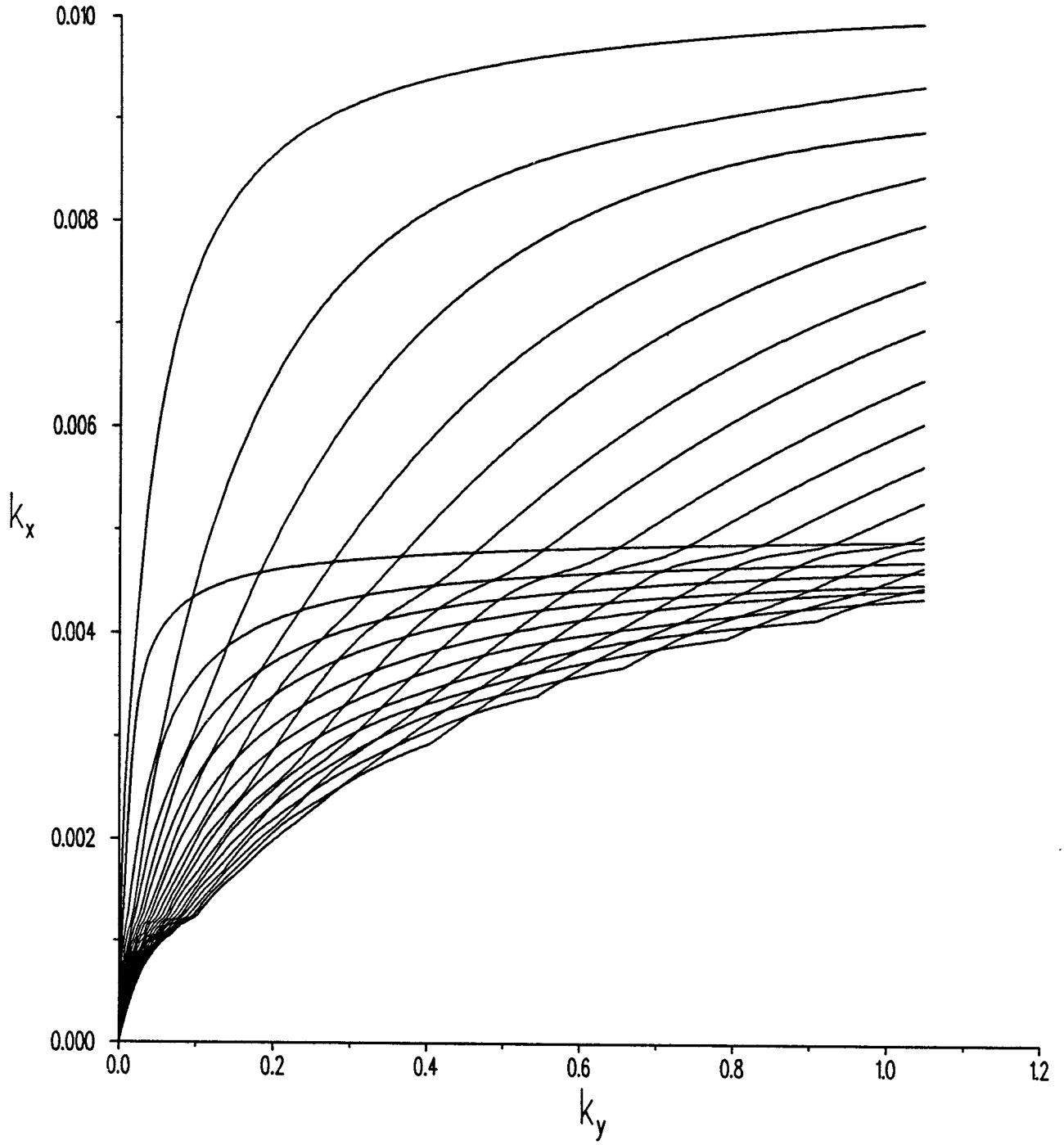

Figure 7. Plots of the first 21 eigencurves in the horizontal wavenumber plane for a source moving at 2.5 ms^{-1}. This is faster than all of the phase speeds of the internal waves, and so all pass through the origin. Units for both axes are rad m^{-1}.

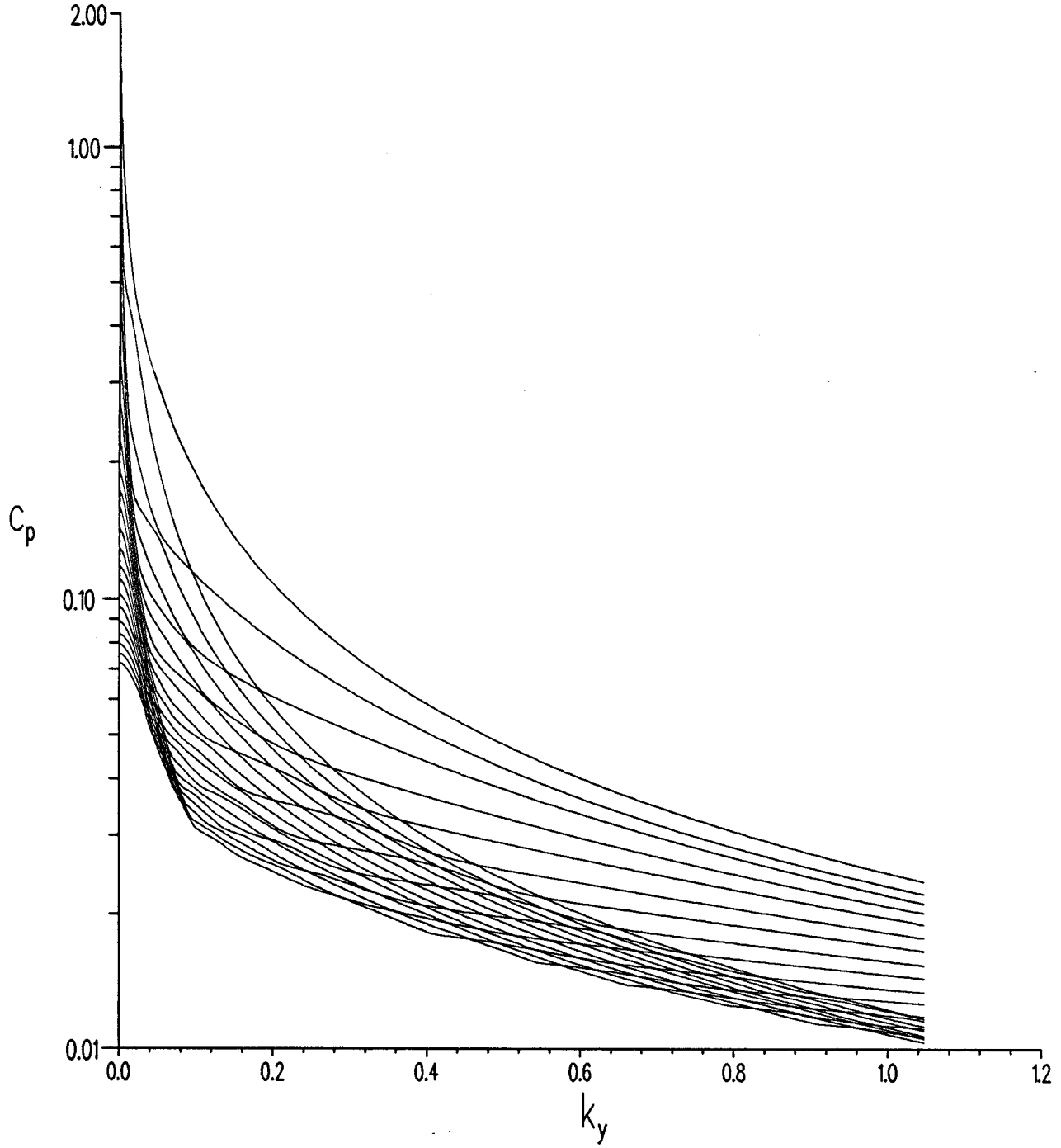

Figure 8. Phase velocities (ms^{-1}) for the curves depicted in Figure 7, plotted as function of cross-track wavenumber (rad m^{-1}).

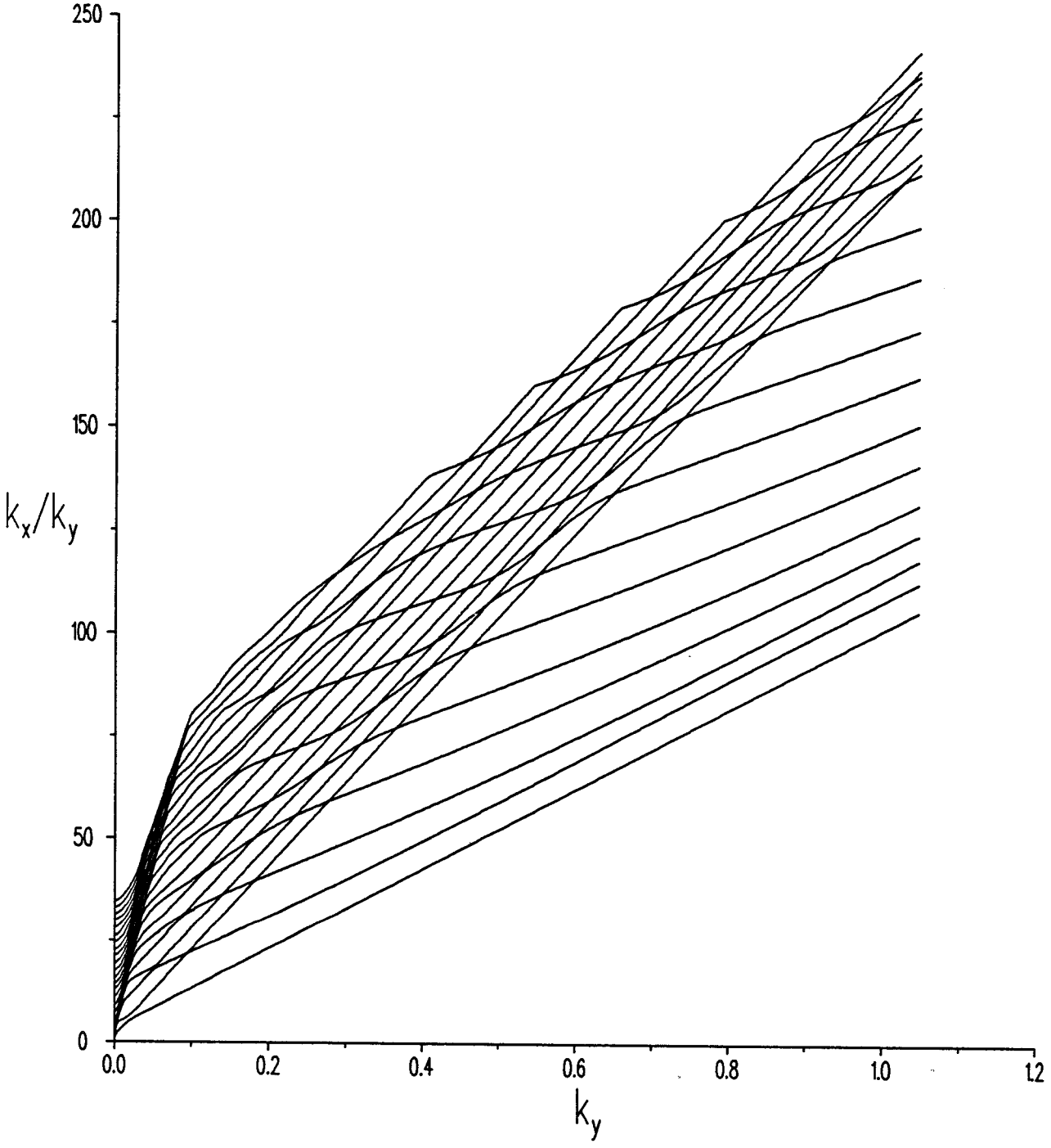

Figure 9. Ratios of k_x/k_y for the curves of Figure 7, plotted as a function of k_y. These are all nonzero for $k_y=0$, indicating that all internal wave elements have a cross-track component to their propagation direction and so form a diverging wake.

mode. The fact that they are all non-zero indicates the expected results that all waves in the wake are divergent; there are no transverse components.

Plots similar to the above were also computed for the lower source speed $c_o = 0.5\ ms^{-1}$. From Figure 8, it is evident that for this source speed, three sub-Froude modes ($c_o < c_m(0)$) would be expected in this case. Plots of $k_{xm}(k_y)$ vs k_y for this combination are shown in Figure 10. The upper three curves exhibit the expected non-zero k_x-values as k_y approaches zero - these correspond to modes containing transverse wave systems whose longest components have crests oriented across-track. The associated phase velocities for this source speed are shown in Figure 11, and show the effect of the pole constraint $|c_o k_x| = |k c_p|$ which implies that $|c_p| \leq |c_o|$ - the upper three curves are clearly forced to a limit at the source speed $c_o = 0.5 ms^{-1}$.

(k) Computation of the Fields

The final step is the numerical implementation of (6.14a). As noted earlier, the integral itself is computed by FFT methods, and so for any fixed values of (x,z), it is very efficient to compute many y-values. However, the problem of computation of extensive sets of field points requires some consideration for efficient computation. Implementation of the methods of this report has been mainly concerned with construction of horizontal (x,y) or vertical (y,z) sections of the fields at a fixed value of the third coordinate. These are conveniently visualized as two-dimensional "images" on a video display, for example.

Since the output fields are real, it suffices to compute only the positive half of the k_y spectra. If the physical fields are to be computed on N_y y-points with uniform spacing Δ_y, the spectra are then computed (sampled) on the points $\{k_{yj} = 2\pi j/(N_y \Delta_y);\ j=0,\ldots,N_y/2-1\ \}$. FFT inversion will then give a representation of the physical fields on periodically replicated sets of values $\{y_q,\ q=1\ldots N_y\}$. For this set of k_y values, the

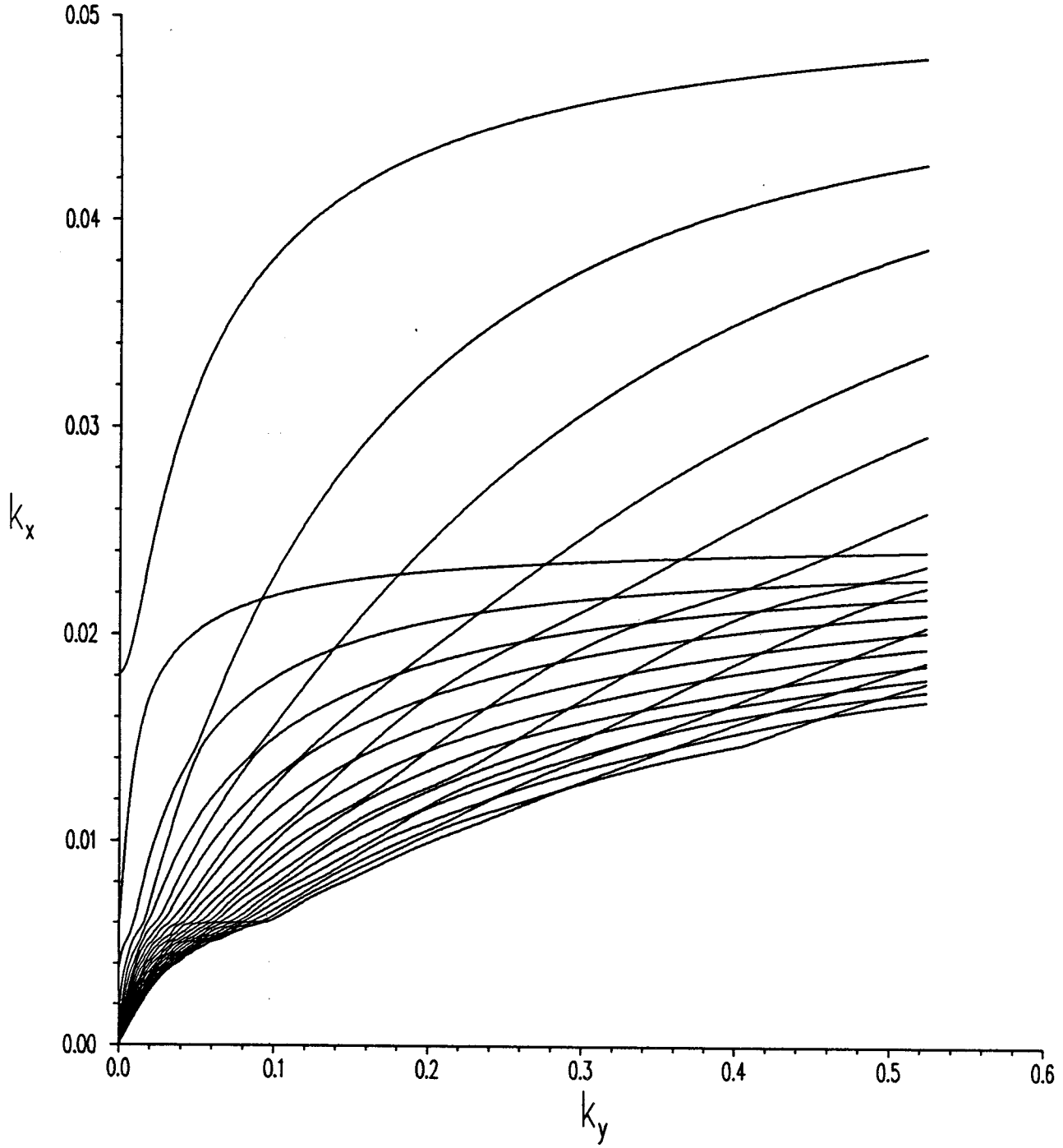

Figure 10. Similar to Figure 7, but for the slower source speed $0.5ms^{-1}$. This is slower than the zero-wavelength phase speeds for the first three modes, and so the corresponding values of k_x are non-zero. This gives rise to transverse components in the wake.

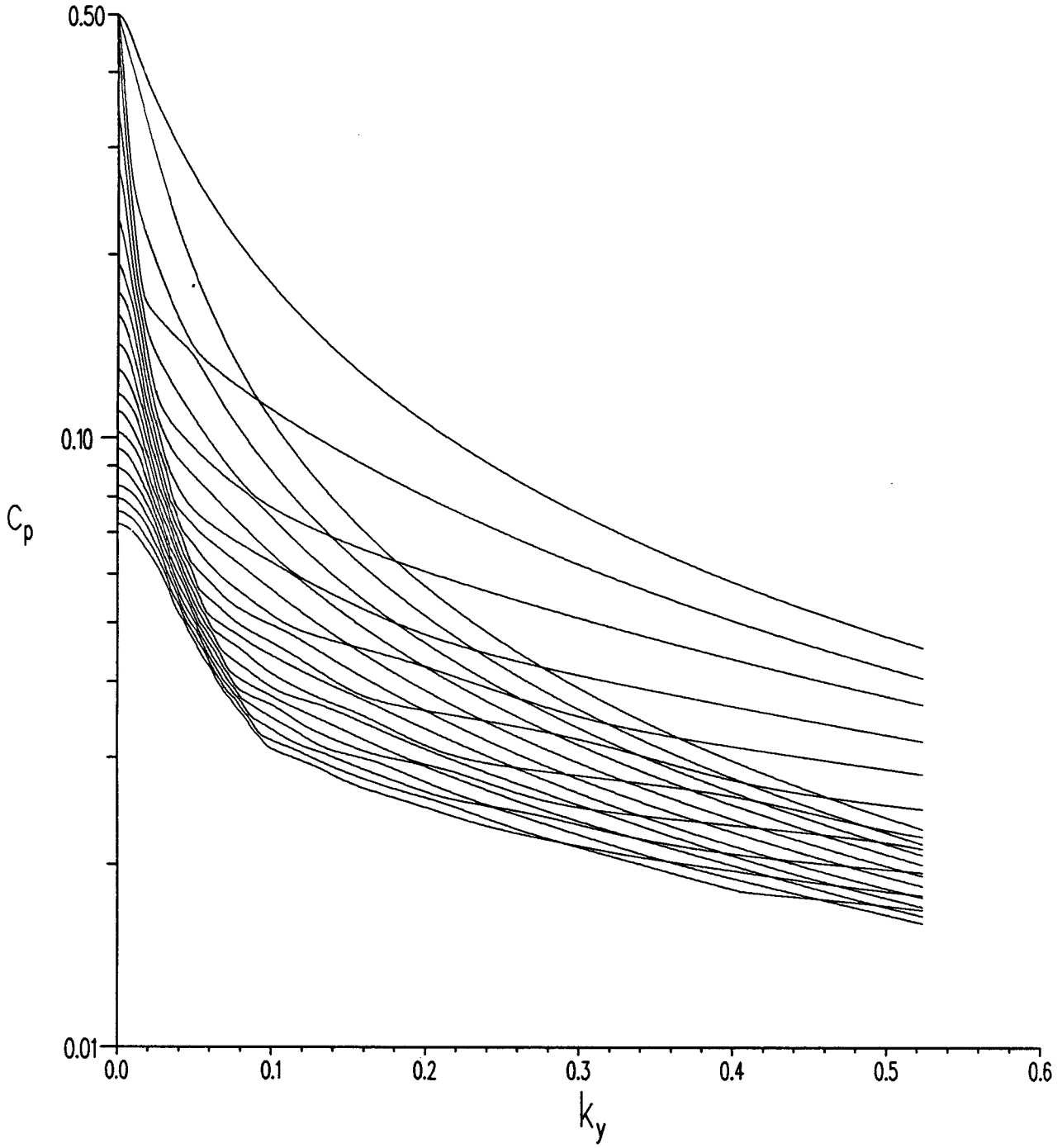

Figure 11. Phase speeds for Figure 10. Note that the moving source constraint forces the phase speeds to be no greater than the source speed.

three sets of eigenvalues (real, imaginary, and zero) corresponding to the three classes of k_x-poles of (6.15), may be computed once for a given profile and source speed, and saved for future use.

This data set is independent of source details and spatial coordinates. Thus it may be used repeatedly for different source models, source depth, and 'observation' coordinates. The eigenfunctions are computed as needed at run-time - the amount of data (modes × k_y-values × layers) is too great to justify saving. In general it will be desired to compute the fields on a set of values $\{x_p,\ p=1...N_x\}$ and $\{z_r,\ r=1...N_z\}$. As there is some numerical expense involved in construction of eigenfunctions, it is therefore most efficient to construct, at run-time, arrays (cf (6.14a)) of the general form $\{\ \bar{f}(x,k_{yj},z_r);\ j=0...N_y/2-1,\ r=1...N_z\ \}$. These are then inverted. Computation of many x-values entails computation of exponentials of the form $\exp(-ixk_x)$. These also prove to be a significant computational expense since there is one k_x-value for each k_y and mode number in each mode set. Significant efficiency[6] is therefore realized by computing fields on a uniform set of x-values with spacing Δ_x. The pair of two-dimensional arrays $\exp[-ix_1k_{xm}(k_y)]$ and $\exp[i\Delta_x k_{xm}(k_y)]$ may be evaluated at run time, and successive x-values obtained by multiplication using

$$\exp[-i(x-\Delta_x)k_x] = \exp[-ixk_x]\ \exp[+i\Delta_x k_x].$$

Sample results will be displayed in the next section.

8. WAKE EXAMPLES

This section is concerned with presentation of some examples of fluid dynamical fields computed from the methods described thus far. For purposes of illustration, the example calculations will be mostly based on a simple Rankine doublet[5,6], consisting of a point source of strength 'm' at x=+a and a sink of equal strength at x=-a. In the notation of Equation (4.1), the mathematical description is

$$S_o(x,y) = m\delta(y)[\ \delta(x-a) - \delta(x+a)], \tag{8.1}$$

hence

$$\hat{S}(k) = (im/\pi)\ \sin(ak_x).$$

It is possible[5] to fit the parameters {m,a} to the diameter and length of solid body with rotational symmetry about its long axis. For illustrative purposes, the values of 100m and 8m have been used for the length and diameter respectively. All examples in this Section will be based on the profile of Figure 2. The two source speeds $2.5ms^{-1}$ and $0.5ms^{-1}$ used for discussion purposes above will be considered for source depths z_s = 35m and z_s = 124m, corresponding to the centres of the upper and lower thermoclines. As well as the independent fluid fields (u,v,w,ζ), the total energy per unit volume

$$E(x,y,z) \equiv \rho_o(z)\ (\ u^2 + v^2 + w^2 + N^2\zeta^2\ )\ /\ 2. \tag{8.2}$$

in the wake is also of interest. For the source (8.1), Equation (6.22) is appropriate. Computations for all of the examples in this Section are based on (6.22), incorporating the first 21 terms in each of the three infinite sums there.

Example 1 considers the fields generated at the surface by the above doublet source travelling at the slower speed in the upper thermocline. Due to the boundary conditions, w and ζ are both zero, and so

only the horizontal currents u(x,y,0) and v(x,y,0) are present. These were computed for a two-dimensional set of x and y values. The results are displayed in Figure 12 as pseudo-images, wherein the grey level corresponds to (signed) current value, white being the largest, and black the smallest. Computations were done at a uniform spacing of 6m in both x and y-directions. There are 512 samples in the along-track direction and 1024 samples across-track. The physical size of the image is from -2.691km to 0.375km along-track, and from -3.072km to 3.066km across-track. The centre of the source is at x=y=0 in the reference frame chosen. Results have been zeroed between the leading and trailing edges of the source in accordance with the range of validity of Equations (6.15). To produce acceptable images it is necessary to clip the data to some desired range, and map this range onto the available 256 grey levels of the display unit. In addition, it proved desireable to take the logarithm of the energy density image prior to the scaling process. Table I contains values of the actual computed

TABLE I.

DATA AND IMAGE RANGES FOR FIGURE 12.

Field:	u (mm s^{-1})	v (mm s^{-1})	$\log_{10}$ E (mj m^{-3})
minimum	-0.408	-1.402	0
maximum	+2.690	+1.402	0.559
black	-0.120	-0.120	-7.0
white	+0.120	+0.120	-4.0

maximum and minimum value for each of the fields u,v, and $\log_{10}$E, as well as the values corresponding to black and white on the images, to which out-of-range values have been clipped.Points to note include the transverse waves clearly visible in the along-track velocity component, and the localized

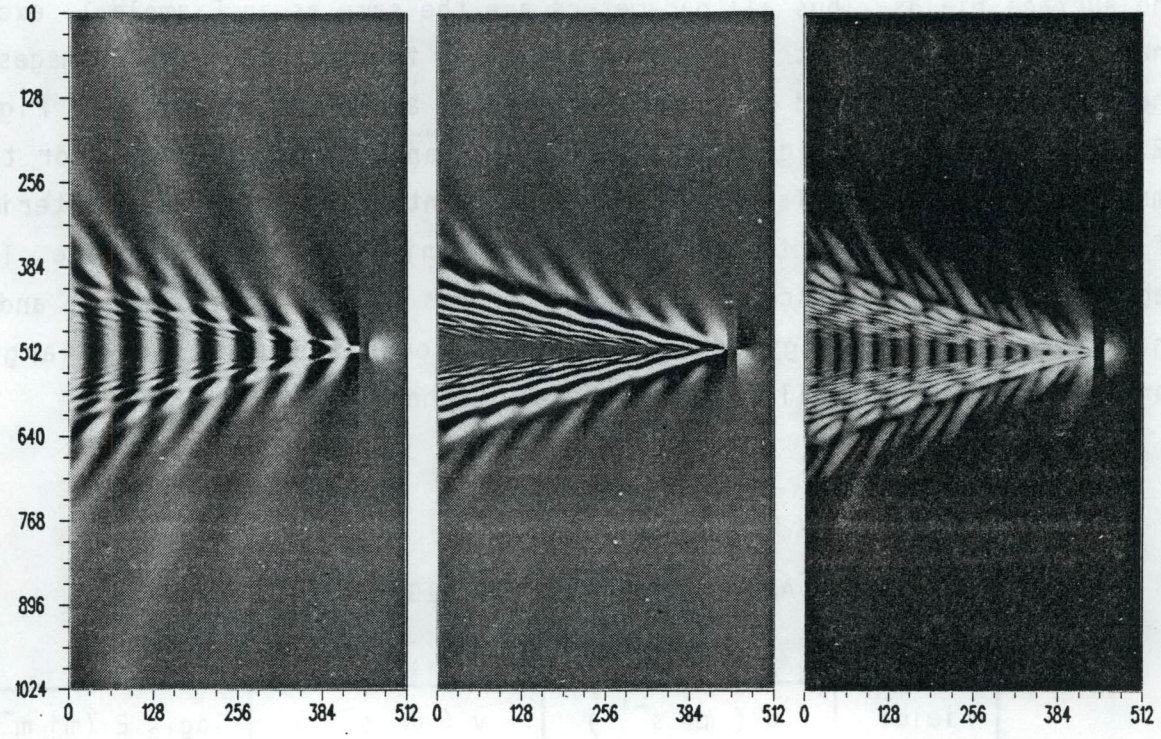

Figure 12. Representations of the surface current components generated by a Rankine doublet source moving at 0.5ms^{-1} in the upper thermocline. The left-hand image is for the along-track current and the central one for the cross-track component. Scaling values are indicated in Table I. Note the presence of the expected transverse waves associated with the first three modes as explained in the text. The image size covers roughly 3 km along-track by 6 km cross-track at 6m steps as explained in the text. The images have been zeroed between the extremes of the source, where the integration by residues breaks down. Note the localized disturbance near the source arising from inclusion of the imaginary modes. The right-hand image represents the (base 10) logarithm of the energy density in the wake.

disturbance in the vicinity of the source. Evidently, most of the energy density at the surface is in the divergent waves. There is also significant energy density in the local disturbance.

Example 2 is intended to illustrate the effect of source depth on the surface fields. Thus all parameters are the same as in Example 1, except that the source is now travelling in the lower thermocline. Pseudo-images of the surface velocity and $\log_{10}$ energy density, analogous to those of Figure 12, are presented in Figure 13. Data ranges and clipping values for this image set are given in Table II. The main point to note is the 'filtering' of shorter wave components by the interior minimum in the N^2 profile. This region has higher evanescence for shorter waves (higher wavenumbers), and so short wave-length energy generated in the lower thermocline is largely confined there - this will be illustrated further below.

TABLE II.

DATA AND IMAGE RANGES FOR FIGURE 13.

Field:	u (mm s^{-1})	v (mm s^{-1})	$\log_{10}$ E (mj m^{-3})
minimum	-0.292	-0.611	0
maximum	+1.096	+0.611	-0.221
black	-0.200	-0.060	-7.0
white	+0.200	+0.060	-4.0

Example 3 is meant to demonstrate the effect of increasing source speed, and uses the higher value $c_o = 2.5 ms^{-1}$. Other conditions remain as in Example 1. With reference to Equation (7.12), it is evident that the effect of increasing c_o is to decrease the parameter s_c. Thus the constraint hyperbolae (7.16a) are all shifted toward smaller values of p and hence k on account of (7.13). But since k_y is constant, the effect is to reduce k_{xn} at

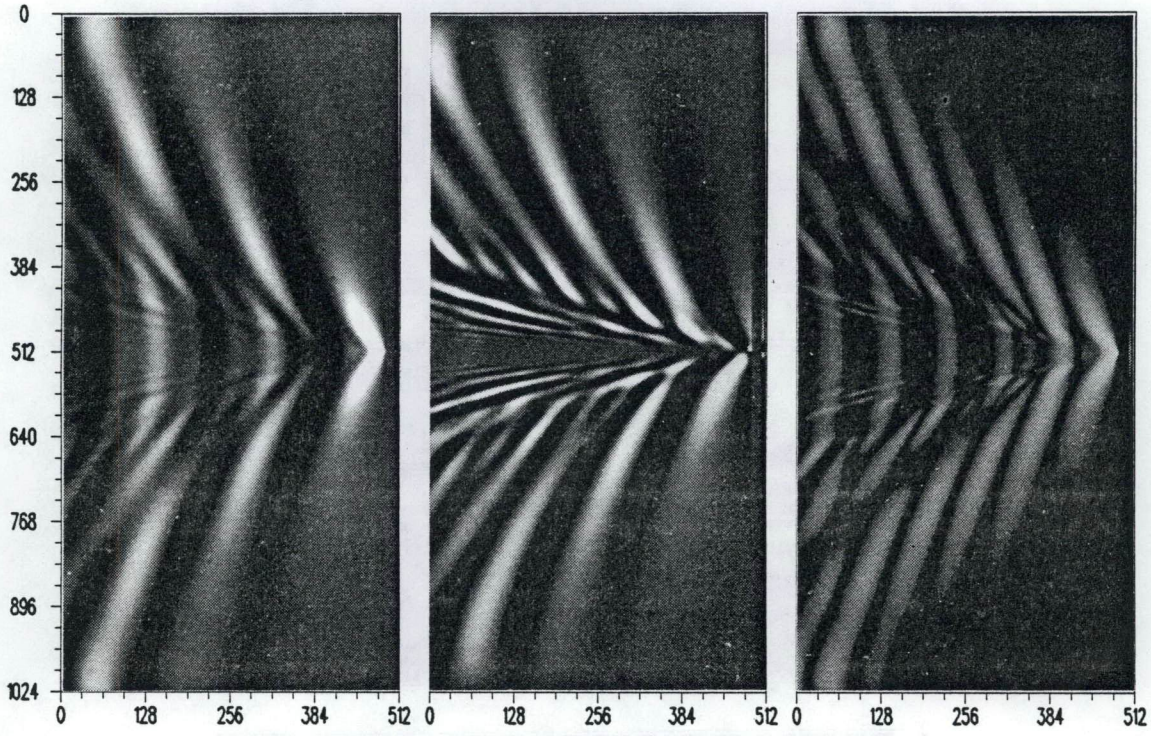

Figure 13. As in Figure 12, but for a source moving in the lower thermocline. Note the filtering of shorter waves due to the interior minimum in the stability profile.

each k_y. Thus every Fourier component **k** in the wake propagates at an angle directed more closely to the cross track axis, and the 'V' patterns defined by the wake become narrower. To accommodate this lengthening of the image, computations were done on a different mesh, specifically a uniform sample length of 3m in both x and y-directions. There are 1024 samples in the along-track direction and 512 samples across-track. The physical size of the image is from -2.8665km to 0.2025km along track, and from -0.768km to 0.765km across track. Surface field images are shown in Figure 14, with data range and clipping values given in Table III. There is clearly no transverse component to the wake, as expected. Also, note the greatly increased effect

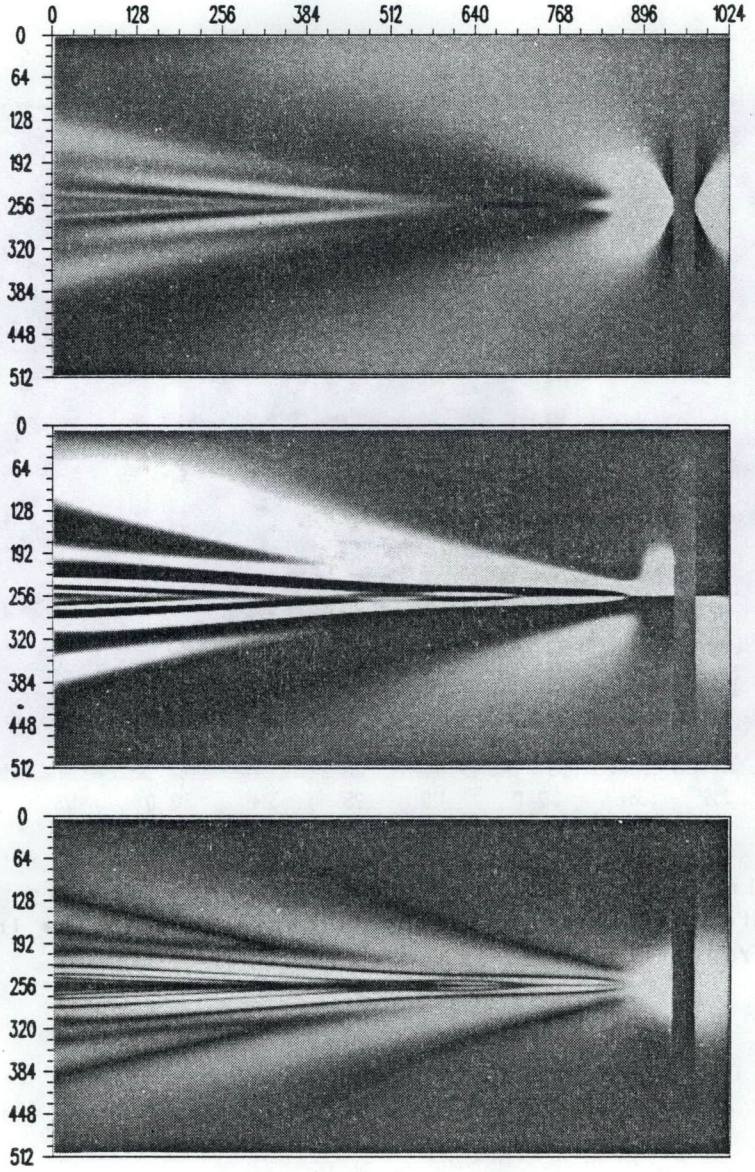

Figure 14. As in Figure 12, but for a source moving at $2.5ms^{-1}$. Pixels here cover 3m by 3m, while the total image covers roughly 3km along-track, and 1.5km across-track. The localized disturbance is stronger due to the larger source strength of the doublet source. As expected, only diverging waves appear in the wake.

of the localized disturbance. The source strength m of the doublet is roughly proportional to the source speed, and therefore results in an increased local flow near the source.

TABLE III.

DATA AND IMAGE RANGES FOR FIGURE 14.

Field	u (mm s^{-1})	v (mm s^{-1})	$\log_{10}$ E (mj m^{-3})
minimum	-0.171	-4.901	0
maximum	+9.304	+4.901	1.636
black	-0.020	-0.020	-8.0
white	+0.020	+0.020	-5.0

The next two examples deal with vertical sections through two of the above wakes. Both examples are for the lower source speed, and correspond to the two source depths. The vertical sections are taken at x = -5.5km. The fields were computed on the same y-points as for Example 1, i.e. 1024 points at 6m steps. Vertical coordinates consist of 512 points at 1m separation, beginning at z=0. This vertical range was chosen for ease of display, and covers only the upper portion of the water column. For these sections, all of the fluid dynamical fields are present, and may be conveniently presented in the form of images as above.

Example 4 is as just described, with the source in the lower thermocline. The upper four images of Figure 15 represent (u,v,w,ζ), with scaling values given in Table IV. The vertical direction represents depth, while the horizontal direction represents cross-track distance. These

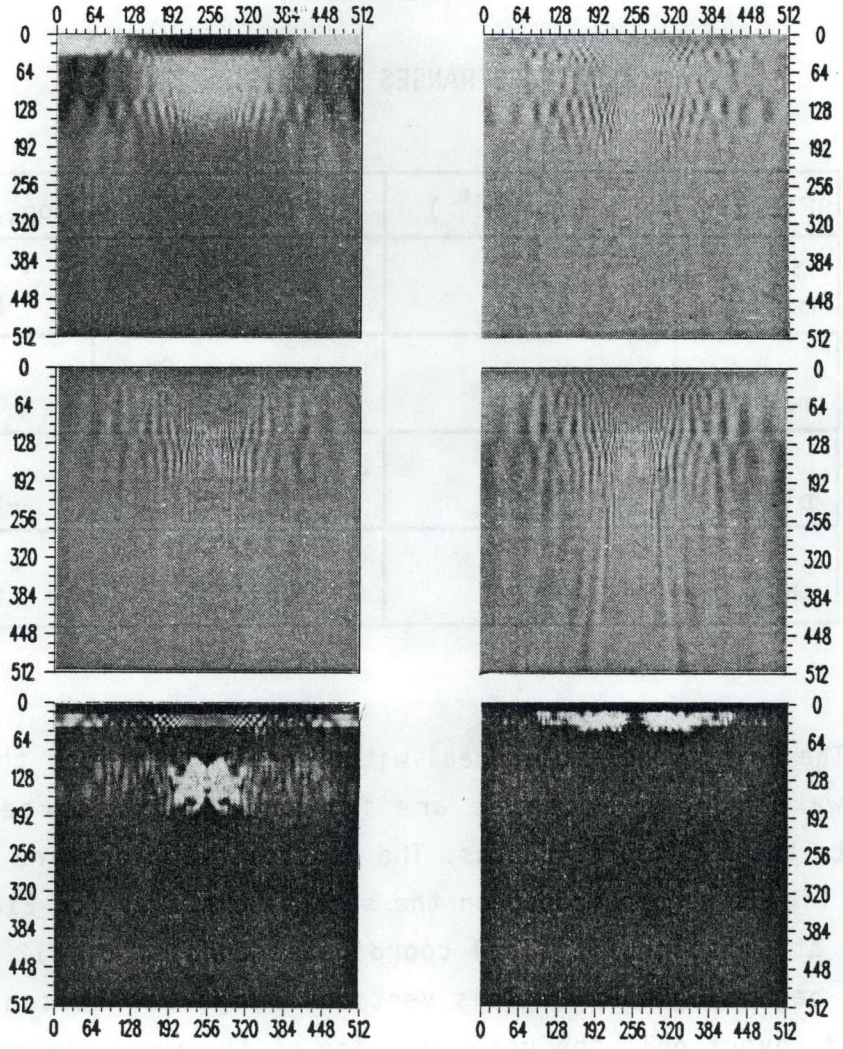

Figure 15. Portions of a vertical section through the wake of Figure 13, at a distance of 5.5km downstream from the source. From top to bottom, and left to right, the first five images depict the fluid velocity components u,v,w, the isopycnal displacement ζ, and the energy density E. The images cover the central 3 km across-track (horizontal) in the upper 511 m of the water (vertical). Note that most of the energy is confined to the lower thermocline where the source is travelling. Longer waves are excited on the upper thermocline. The lower right image shows the energy density, on the same coordinates, for a source moving in the upper thermocline as in Figure 12.

TABLE IV.

Data and image ranges for Figure 15.
E_1 is for the deeper source, E_2 for the shallow one.

Field	Minimum	Maximum	Black	White
u (mm/s)	-0.107	+0.165	-0.107	+0.165
v (mm/s)	-0.395	+0.395	-0.395	+0.395
w (mm/s)	-0.641	+0.657	-0.641	+0.657
ζ (cm)	-5.977	+6.503	-5.977	+6.503
E_1(mJ/s)	1.4×10^{-6}	0.233	1.4×10^{-6}	0.045
E_2(mJ/s)	4.7×10^{-8}	8.545	4.7×10^{-8}	0.489

sections were computed on the basis of 1024 cross-track points, but only the central 512 y-points, with indices from 256 to 767, are displayed. Note the disparate (6-to-1) scales along the two directions. The associated energy density in the vertical section is shown in the lower left image. Clearly, the higher frequencies are confined to the lower thermocline. There is however, significant 'leakage' of longer wavelength energy into the upper thermocline (which has a higher stratification than the lower one). This longer wavelength energy is in fact what makes its presence felt at the surface, as shown in Figure 13. Example 5, consists of the same model, but with the source in the upper thermocline. The lower right image of Figure 15 shows the energy density, on the same coordinates as for Example 4. This represents a vertical section through the wake of Figure 12. The energy is clearly confined almost entirely to the upper thermocline. The velocity and

displacement fields are not depicted for Example 5, but for reference, the ranges of these components are given in Table V.

TABLE V.

DATA RANGES FOR THE FIELD COMPONENTS OF EXAMPLE 5

Field	Minimum	Maximum
u (mm/s)	-0.227	0.285
v (mm/s)	-2.76	2.76
w (mm/s)	-1.84	1.74
ζ (cm)	-15.6	15.1

9. Comparison With Measured Data

As a final example, a comparison with measured data is considered. The details of the measurements are discussed in detail elsewhere[1]. Basically a surface ship (CFAV Endeavour) generated a divergent internal wave wake by steaming in a straight line at constant speed. After a time, the ship made a wide turn, and made a measurement cut across its own wake. The data of interest for present purposes were obtained from current meters mounted ahead of the bow at a nominal depth of 1m. Ship position information was obtained from a trio of shore-based trisponders. The measured current velocity data were reduced to a component along the measurement ship's track. Those data are displayed in Figure 20 of Reference 1.

Model currents were computed using a layered representation of the profile contained in the above reference, under all of the assumptions and simplifications discussed earlier. The source type used was a more complicated one[29] than the simple Rankine doublet. The measured positions at which current data were available were converted into positions relative to the steady state coordinate system of the present model. The synthetic current data were then sampled along this track and converted to a component along the measurement track to produce a data set which may be directly compared with the measured data. The results of the comparison are presented in Figure 16. The measured data is the lighter curve, while the darker curve represents the model data. The data, in units of ms^{-1}, are plotted as a function of measurement time. It is evident that in this case at least, reasonable agreement was obtained. The predicted amplitudes agree well, although the wavelengths are perhaps slightly longer than measured. Considering all of the approximations in the model, and the physical realities of the experimental situation, the agreement serves as at least an indication that linearized internal wave theory is capable of realistic predictions.

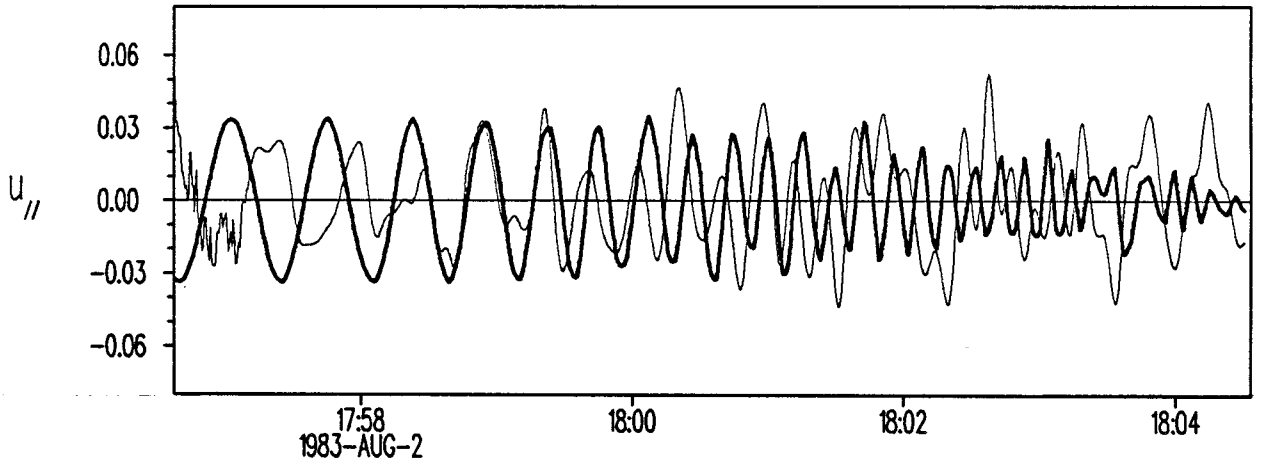

Figure 16. Comparison of internal wave currents predicted by the model with measured data. The lighter curve represents data measured in the internal wave wake of a surface ship. Corresponding data predicted from the model are given by the dark curve. The current is the component along the measurement track (ms^{-1}) as a function of measurement time.

10. Concluding Remarks

It has been demonstrated that linearized inviscid internal wave theory is capable of providing realistic internal wave field estimates in an efficient and straightforward manner. Relatively simple modifications to standard normal mode expansion techniques permit inclusion of both the radiating and near-field contributions. These modifications also provide an alternative Green's function representation, which has a higher rate of convergence in the modal sums. All pertinent fluid dynamical variables can be easily computed together.

It is also demonstrated that profiles possessing multiple thermoclines need not cause major difficulties. For certain wavenumber regimes, such profiles will possess regions of high evanescence, a common cause of "instability" in eigenfunction computations. Such profiles will generally cause multiple roots to arise in the Wronskian in a numerical scheme. Appropriate modifications to the concept of an eigenfunction expansion are readily introduced to handle such profiles, and properly account for trapping of energy generated with a thermocline.

REFERENCES

1. B.A.Hughes and T.W.Dawson,"Joint CAN/US Ocean Wave Investigation Project. DREP Measurements of Surface-Ship Produced Internal Wave Wakes in Knight Inlet, B.C. 1983", DREP Technical Memorandum 85-20, Defence Research Establishment Pacific, Forces Mail Office, Victoria B.C., Canada, V0S 1B0, 1985.

2. A.H. Schooley and B.A.Hughes, "An Experimental and Theoretical Study of Internal Waves Generated by the Collapse of a Two-Dimensional Mixed Region in a Density Gradient", J. Fluid Mech., 53, 159-175, 1972

3. J.M. Bergin, "Internal Wave Generation Caused by the Growth and Collapse of a Mixed Region", NRL Report 7568, Naval Research Laboratory, Washington D.C., 1973.

4. John W. Miles, "Internal Waves Generated by a Horizontally Moving Source", Geophysical Fluid Dynamics, 2, 63-87, 1971.

5. L.M. Milne-Thomson, "Theoretical Hydrodynamics", 3rd ed., MacMillan & Co. Ltd., London, 1955.

6. Michael Milder, "Internal Waves Radiated by a Moving Source. Volume I - Analytic Simulation", RDA-TR-2702-007, R&D Associates, PO Box 3580, Santa Monica, CA 90403, Feb. 1974.

7. P.H. LeBlond and L.A.Mysak, "Waves in the Ocean", Elsevier Scientific Publishing Company, 1978.

8. James Lighthill, "Waves in Fluids", Cambridge University Press, Cambridge, 1978.

9. Robert D. Mager, "Internal Gravity Waves Generated by a Moving Source in a Stratified Fluid", University of Denver, Denver Research Institute, Report MS-R-7502, 1974

10. James A. Young, Robert K.-C. Chan, James Riley, and Denny Ko. "Development of an Internal Wave Computer Code", Science Applications, La Jolla, California, Report SAI-74-598-LJ, 1974.

11. Henrik Schmidt and Finn B. Jensen, "An Efficient Numerical Solution Technique for Wave Propagation in Horizontally Stratified Ocean Environments", SACLANTCEN Memorandum SM-173, August, 1984.

12. "Oceanographic Observations at Ocean Station P, 27 July - 13 September, 1972, Volume 102", Pacific Maritime Report 81-16, Institute of Ocean Sciences, Victoria, B.C., 1981.

13. O.M. Phillips, "The Dynamics of the Upper Ocean", 2nd ed., Cambridge University Press, Cambridge, 1977.

14. G.K. Batchelor, "An Introduction to Fluid Dynamics", Cambridge University Press, Cambridge, 1967.

15. Philip M. Morse and Herman Feshbach, "Methods of Theoretical Physics", McGraw-Hill Book Company, Inc., New York, 1953.

16. William E. Boyce and Richard C. DiPrima, "Elementary Differential Equations and Boundary Value Problems", John Wiley & Sons,Inc., New York, 1969.

17. Allan D. Pierce, "Propagation of Acoustic-Gravity Waves in a Temperature- and Wind-Stratified Atmosphere", J. Acoust. Soc. Amer., 37, 281-227, 1965.

18. Michael Porter and Edward L. Reiss, "A Numerical Method for Ocean-Acoustic Normal Modes", J. Acoust. Soc. Amer., 76, 244-252, 1984.

19. Michael Milder, "User's Manual for the Computer Program ZMODE", RDA-TR-2701-001, R&D Associates, PO Box 3580, Santa Monica, CA 90403, July 1973.

20. Thomas H. Bell, Jr., "Numerical Calculation of Dispersion Relations for Internal Gravity Waves", NRL Report 7294, Naval Research Laboratory, Washington D.C., 1971.

21. E. Ammicht and D.G. Stickler, "Uniform Asymptotic Evaluation of the Continuous Spectrum Contribution for a Stratified Ocean", J. Acoust. Soc. Amer., 76, 186-191, 1984.

22. Allan D. Pierce, "The Multilayer Approximation for Infrasonic Wave Propagation in a Temperature- and Wind-stratified Atmosphere", J. Comp. Phys., 1, 343-366, 1967.

23. Myron Fliegel and Kenneth Hunkins, "Internal Wave Dispersion Calculated Using the Thomson-Haskell Method", Journal of Physical Oceanography, 5, 541-548, 1975.

24. C.O. Hines, " A Critique of Multilayer Analyses in Application to the Propagation of Acoustic-Gravity Waves", J. Geophys. Research, 78, 265-273, 1973.

25. Dale D. Ellis, "A Two-Ended Shooting Technique for Calculating Normal Modes in Underwater Acoustic Propagation", DREA Report 85/105, Sept. 1985.

26. R.C.Y.Chin, G.W.Hedstrom and L.Thigpen, "Matrix Methods in Synthetic Seismograms", Geophys. J.R. Astr. Soc., 77, 483-502, 1984.

27. Gary Brooke, DREP, private communication, 1987.

28. Ghislain R. Franssens, "Calculation of the Elasto-Dynamic Green's Function in Layered Media by Means of a Modified Propagator Matrix Method", Geophys. J.R. Astr. Soc., 75, 669-691, 1983

29. B.A. Hughes, DREP, private communication.

DISTRIBUTION

REPORT: DREP REPORT 88-7

TITLE: The DREP Internal Wave Normal Mode Model-Theoretical Background.

AUTHOR: T.W. Dawson

DATED: April 1988

SECURITY GRADING: UNCLASSIFIED

3 - DSIS
Circulate to:
DRDM
DSP

1 - DREV
1 - DREO
1 - DREA

1 - ORAE Library
1 - D Met Oc
1 - Maritime Tech Library
1 - Bedford Inst of Oceanography
Library
1 - NRC
1 - RRMC Dept of Oceanography
1 - RMC
1 - CRC Library

1 - CDLS(L) CDR
1 - CDLS(W) CDR
1 - DRA Paris

1 - Great Lakes Inst.
University of Toronto

1 - Canada Centre for Inland Waters
Burlington, ON L7R 4A6
Attn: Mr. Mark A. Donelan

AUSTRALIA

1 - Surveillance Systems Group
Electronics Research Laboratory
G.P.O. Box 2151
Adelaide, S. Australia 5001
Attn: Dr. D. Cartwright

BRITAIN

Ministry of Defence
1 - DRIC

UNITED STATES

3 - DTIC
1 - Naval Research Laboratory
Washington, D.C. 20375
1 - Environmental Research Inst.
of Michigan
P.O. Box 8618
Ann Arbor, Michigan 48107
Attn: Dr. R. Shuchman

3 - Applied Physics Laboratory
Johns Hopkins Road
Laurel, MD 20707
1 - Dr. R. Gasparovic
1 - Dr. R. Gotwols
1 - Dr. D. Thompson

2 - Naval Ocean Systems Center
San Diego, CA 92152
1 - Dr. R.R. Buntzen
1 - Dr. R.R. Hammond

2 - TRW Inc.
1 Space Park
Redondo Beach, CA 96278
1 - Dr. B. Lake
1 - Dr. K. Kwoh

1 - Dynamics Technology Inc.
1815 N. Lynn St.
Suite 801
Arlington, VA 22209
Attn: Dr. S. Borchardt

.../2

DISTRIBUTION LIST
(Continued)

1 - Dr. R.S. Winokur
Assoc. Technical Director for
Ocean Science and International Program
Office of Naval Research
Arlington, VA 22217

1 - Defence Advanced Research
Projects Agency,
1400 Wilson Blvd.
Arlington, VA 22209

1 - R&D Associates
P.O. Box 9695
Marina Del Ray, CA 90291
Attn: Dr. D. Holliday

1 - Institute of Geophysics and
Planetary Physics, A-025
Scripps Institution of
Oceanography
La Jolla, CA 92093
Attn: Prof. W. Munk

1 - Dr. Arthur Reed
9106 Warren Street
Silver Spring, MD 20910

DOCUMENT CONTROL DATA

(Security classification of title, body of abstract and indexing annotation must be entered when the overall document is classified)

1. ORIGINATOR (the name and address of the organization preparing the document. Organizations for whom the document was prepared, e.g. Establishment sponsoring a contractor's report, or tasking agency, are entered in section 8.)

Defence Research Establishment Pacific

2. SECURITY CLASSIFICATION (overall security classification of the document. including special warning terms if applicable)

Unclassified

3. TITLE (the complete document title as indicated on the title page. Its classification should be indicated by the appropriate abbreviation (S,C,R or U) in parentheses after the title.)

The DREP Internal Wave Normal Mode Model-Theoretical Background (U)

4. AUTHORS (Last name, first name, middle initial)

T. W. Dawson

5. DATE OF PUBLICATION (month and year of publication of document)

6a. NO. OF PAGES (total containing information. Include Annexes, Appendices, etc.)

6b. NO. OF REFS (total cited in document)

29

7. DESCRIPTIVE NOTES (the category of the document, e.g. technical report, technical note or memorandum. If appropriate, enter the type of report, e.g. interim, progress, summary, annual or final. Give the inclusive dates when a specific reporting period is covered.)

Technical Memorandum 88-7

8. SPONSORING ACTIVITY (the name of the department project office or laboratory sponsoring the research and development. Include the address.)

DREP

9a. PROJECT OR GRANT NO. (if appropriate, the applicable research and development project or grant number under which the document was written. Please specify whether project or grant)

DRDM-04

9b. CONTRACT NO. (if appropriate, the applicable number under which the document was written)

10a. ORIGINATOR'S DOCUMENT NUMBER (the official document number by which the document is identified by the originating activity. This number must be unique to this document.)

Technical Memorandum 88-7

10b. OTHER DOCUMENT NOS. (Any other numbers which may be assigned this document either by the originator or by the sponsor)

11. DOCUMENT AVAILABILITY (any limitations on further dissemination of the document, other than those imposed by security classification)

- (X) Unlimited distribution
- ( ) Distribution limited to defence departments and defence contractors; further distribution only as approved
- ( ) Distribution limited to defence departments and Canadian defence contractors; further distribution only as approved
- ( ) Distribution limited to government departments and agencies; further distribution only as approved
- ( ) Distribution limited to defence departments; further distribution only as approved
- ( ) Other (please specify):

12. DOCUMENT ANNOUNCEMENT (any limitation to the bibliographic announcement of this document. This will normally correspond to the Document Availabilty (11). However, where further distribution (beyond the audience specified in 11) is possible, a wider announcement audience may be selected.)

no limitation

13. ABSTRACT (a brief and factual summary of the document. It may also appear elsewhere in the body of the document itself. It is highly desirable that the abstract of classified documents be unclassified. Each paragraph of the abstract shall begin with an indication of the security classification of the information in the paragraph (unless the document itself is unclassified) represented as (S), (C), (R), or (U). It is not necessary to include here abstracts in both offical languages unless the text is bilingual).

See Text

14. KEYWORDS, DESCRIPTORS or IDENTIFIERS (technically meaningful terms or short phrases that characterize a document and could be helpful in cataloguing the document. They should be selected so that no security classification is required. Identifiers, such as equipment model designation, trade name, military project code name, geographic location may also be included. If possible keywords should be selected from a published thesaurus. e.g. Thesaurus of Engineering and Scientific Terms (TEST) and that thesaurus-identified. If it is not possible to select indexing terms which are Unclassified, the classification of each should be indicated as with the title.)

Internal Waves
Normal Modes
Layered Approximation
Evanescent Layers
Wakes